Title

Recoil-Proton Polarization in Negative Kaon-Proton Elastic Scattering Between 700 and 1400 MeV/c Incident Kaon Momenta

Author

Wang, Ching Lin

Publication Date

1965-04-01

University of California

Ernest O. Lawrence Radiation Laboratory

Berkeley, California

UCRL-11881

UNIVERSITY OF CALIFORNIA

Lawrence Radiation Laboratory
Berkeley, California

AEC Contract No. W-7405-eng-48

RECOIL-PROTON POLARIZATION IN NEGATIVE KAON-PROTON ELASTIC SCATTERING BETWEEN 700 AND 1400 MeV/c INCIDENT KAON MOMENTA

Ching Lin Wang

(Ph. D. Thesis)

April 19, 1965

RECOIL-PROTON POLARIZATION IN NEGATIVE KAON-PROTON ELASTIC SCATTERING BETWEEN 700 AND 1400 MeV/c INCIDENT KAON MOMENTA

Contents

RECOIL-PROTON POLARIZATION IN NEGATIVE KAON-PROTON ELASTIC SCATTERING BETWEEN 700 AND 1400 MeV/c INCIDENT KAON MOMENTA

Ching Lin Wang

Lawrence Radiation Laboratory
University of California
Berkeley, California

April 19, 1965

ABSTRACT

A negative kaon beam from an internal target of the Bevatron was directed onto a liquid hydrogen target, and the polarization of recoil protons in K^--p elastic scattering was measured at 812, 952, 1050, 1159, and 1266 MeV/c incident kaon momenta.

A scintillation and Cerenkov counter system identified K^--p interactions and triggered a spark chamber array and camera. A cylindrical spark chamber surrounding the hydrogen target was used to identify the elastic scatterings, and a semicylindrical chamber interleaved with carbon and steel absorbers was used to obtain the range and polarization information. The azimuthal asymmetry of the angular distribution of recoil protons which scattered in the carbon plates was observed, and the polarization was estimated by the method of maximum likelihood.

By incorporating the K^--p elastic differential cross sections available from this and other experiments with the polarization obtained here, single-energy phase-shift analyses were made at 21 momenta between 620 and 1350 MeV/c. Furthermore, an energy-dependent phase-shift analysis was made by utilizing all available data on K^--p total cross section, differential cross section, charge-exchange cross section, and the K^--n total cross section between 110 and 1400 MeV/c.

Both the results of single-energy and energy-dependent phase-shift analyses are in agreement with the suggestions of an $F_{5/2}$ resonance for the 1815-MeV bump in the K^--p total cross section; however, a $D_{5/2}$ assignment can fit the data equally well. A $D_{3/2}$ assignment is less favorable, yet it cannot be strongly ruled out. A possible set of energy-dependent phase-shift solutions was obtained by assuming a $D_{5/2}$ (T = 1) resonance at 1765 MeV and an $F_{5/2}$ (T = 0) resonance at 1815 MeV. This set is not unique, however.

I. INTRODUCTION

The K^--p total cross section is known to have a marked peak at about 1.05 BeV/c incident K^- momentum or at 1815 MeV total barycentric energy.[1,2] (See Fig. 1.) It has a relatively broad width of at least 120 MeV, which is in fact difficult to determine because of the asymmetry in the shape. On comparison of the K^--p and K^--n total cross sections, it has been suggested that a resonance in T = 0 isotopic spin state may explain this bump. This was based on the argument that $\sigma\ (K^--p) = 1/2\ [\sigma\ (T = 0) + \sigma\ (T = 1)]$ and $\sigma\ (K^--n) = \sigma\ (T = 1)$. If this resonance were a property of the T = 1 $\overline{K}$-N interaction, it would contribute peaks to both K^--p and K^--n cross sections, in the ratio 1:2. Clearly such a strong peak was not observed in the K^--n cross section, therefore T = 0 holds for the resonance.

The spin of the resonant state is not quite known, although it appears probable that $J \geqslant 3/2$, judging from the magnitude of the peak. At resonance, the total cross section in the resonant state may be written

$$\sigma_t\ (\text{res}) = (1/2)(2J + 1)\ 4\ \pi\ \lambda\!\!\!^{-}{}^2\ (\sigma_{\text{elastic}}/\sigma_{\text{total}})_{\text{res}},$$

where $\pi\ \lambda\!\!\!^{-}{}^2 = 4.18$ mb at 1050 MeV/c.[7] The resonant cross section observed is therefore compatible with $J \geqslant 3/2$.

The parity of the resonant state is not known. Also little is known concerning the processes giving rise to this resonance, although there have been various speculations. At the time this experiment was planned, there were the following two schemes:

a. The peak is one of the two pion-hyperon isobaric states corresponding to the third pion-nucleon resonance (1670) MeV) as predicted by global symmetry.[8] The mass, width, and isotopic spin of the two predicted resonances are (M_1 = 1855 MeV, Γ_1 = 66 MeV, T_1 = 0) and M_2 = 1930 MeV, Γ_2 = 82 MeV, T_2 = 1), respectively. Apparently M_1 is too big and Γ_1 is too small for the observed peak, but such

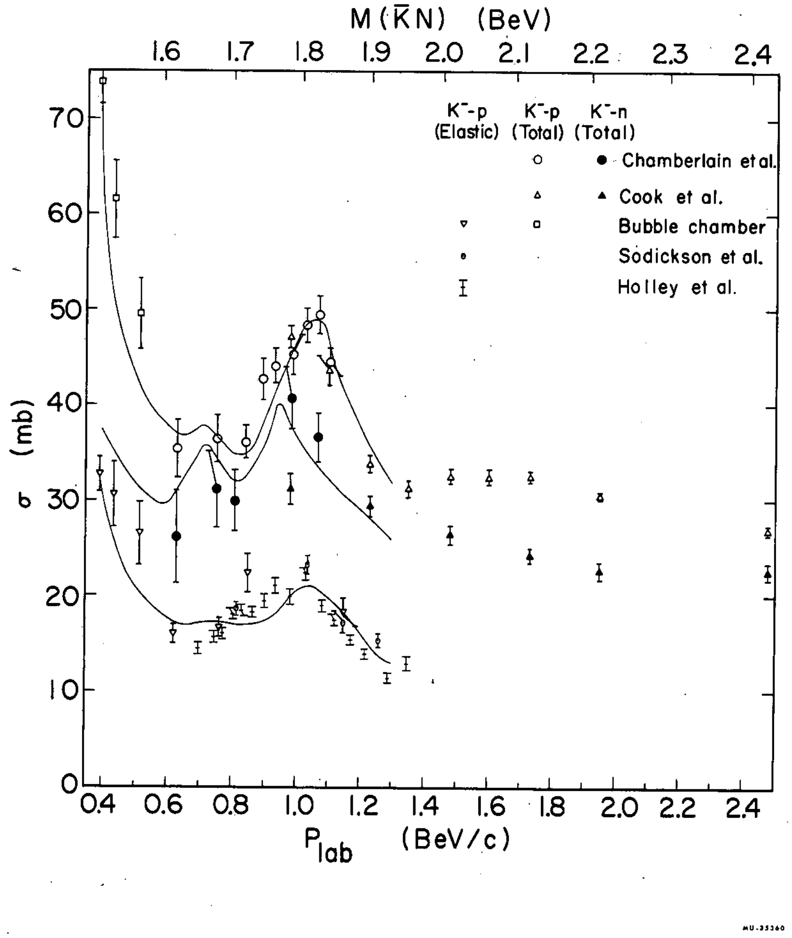

Fig. 1. The K$^-$-p and K$^-$-n total cross section and K$^-$-p elastic cross section measurements available from 0.4 to 2.4 BeV/c incident kaon momenta, taken from the work of Cook et al. (reference 1), Chamberlain et al. (reference 2), Sodickson et al. (reference 3), Holley (reference 4), and bubble chamber experiments.[5,6] The errors of the data by Holley are purely statistical. The curves are theoretical fits obtained by an energy-dependent phase-shift analysis (see Sec. V of text).

discrepancies need not imply disagreement with the idea of global symmetry because of the approximate nature of the scheme. However, no evidence for the $T_2 = 1$ counterpart seems to exist in the K^--n total cross sections. This model predicts that the resonance should be $F_{5/2}$, given odd parity for KΣN.

b. The peak is caused by the rapidly rising inelastic cross section for $K^- + p \rightarrow K^{*-} + p$ (threshold 1812 MeV). Ball and Frazer have shown,[9] by means of partial-wave dispersion relation, how a sharp peak primarily in the $D_{3/2}$ state in K^--p elastic cross section can arise, given that K^* has $J = 1$ and $T = 1/2$.

The main purpose of this experiment was to explore the spin and parity of the resonant state by means of the differential cross section and the recoil-proton polarization measurement. Besides, if one is lucky, the resolution of the spark chamber may be good enough to resolve the multivertex events, such as charge-exchange scattering, $K^- + p \rightarrow \overline{K}^0 + n$, with subsequent decay of $\overline{K}^0 \rightarrow \pi^+ + \pi^-$, K^* production, etc. All these studies should have some bearing on the nature of the resonance.

It was only more recently that new models appeared that might account for the classification of this resonance, namely the Regge trajectories and the SU_3 unitary symmetry. The Y_0^*(1815 MeV) resonance can be considered as the Regge recurrence of the Λ, or as a member of the "excited" (spin 5/2) baryon octet.[10] Thus its spin-parity is predicted to be $J^P = (5/2)^+$, viz., an $F_{5/2}$ resonance. The experimental assignment of the spin and parity of this resonance is therefore of great interest in the light of current theoretical works.

In addition, by the investigation of K^--p invariant mass in the reaction $K^- + n \rightarrow K^- + \pi^- + p$, Barbaro-Galtieri, Hussain, and Tripp have recently suggested[11] that the 1815-MeV bump may actually consist of two adjacent resonances, both of high elasticity. The conjectured resonance parameters were: $M_1 = 1765$ MeV, $\Gamma_1 = 60$ MeV, and χ_1 (= elasticity = Γ_{el}/Γ) = 0.6; $M_2 = 1815$ MeV, $\Gamma_2 = 70$ MeV, and $\chi_2 = 0.8$. This adds further interest in analyzing the data obtained from this experiment.

II. EXPERIMENTAL PROCEDURE

A. Theoretical Basis for the Experimental Method

Because of the existence of the spin-selective nuclear forces in the spin-orbit coupling, the interaction of particles with spin and spinless particles will in general leave the particles with spin partially polarized. This effect is frequently observed in the polarization of protons recoiling from pions impinging on hydrogen, or the polarization of initially unpolarized nucleons scattering off spinless nuclei. As is well known in optics, a polarizer can in turn be used as an analyzer for beams of unknown polarization. Carbon as a polarizer has been most extensively studied and hence most commonly used as an analyzer in high-energy particle scattering.

The differential cross section of protons with polarization P scattering off spinless carbon nuclei is a superposition of two terms: an azimuthally symmetric term $\frac{d\sigma_0}{d\Omega}$, which is essentially the differential cross section of unpolarized proton-carbon scattering, and a term $\frac{d\sigma_0}{d\Omega}$ PA cos ϕ, which is azimuthally asymmetric through the factor cos ϕ; namely,[12]

$$\frac{d\sigma\ (\theta,\phi,E)}{d\Omega} = \frac{d\sigma_0\ (\theta,E)}{d\Omega}\ [1 + PA\ (\theta,E)\cos\phi],$$

where θ and ϕ are respectively the polar and azimuthal angles of the p-C scattering, E is the energy of the incident proton, and A is the <u>analyzability</u> of the carbon nucleus. The product A cos ϕ is referred to as the <u>analyzing power</u> of the p-C scattering.

We now use a statistical interpretation of the differential cross section. For a sample of protons having a polarization P, the probability density function for a p-C scattering occurring at θ and ϕ is

$$w\ (\theta,\phi,E) = \frac{1}{\sigma(E)}\ \frac{d\sigma_0\ (\theta,E)}{d\Omega}\ [1 + PA\ (\theta,E)\cos\phi],$$

where the normalization constant $\sigma\ (E) = \int \frac{d\sigma\ (\theta,\phi,E)}{d\Omega}\ d\Omega$ is the p-C scattering cross section at the incident proton energy E. The total density function W for the occurrence of all the scattering events is then the product of the individual probabilities

$$W = \prod_i F_i [1 + PA(\theta_i, E_i) \cos\phi_i],$$

where

$$F_i = \frac{1}{\sigma(E_i)} \frac{d\sigma_0(\theta_i, E_i)}{d\Omega} .$$

Now according to the statistical method of maximum likelihood,[13] the best estimate of the polarization of the protons is the value of P which makes this product a maximum. In actual computation, one simply constructs the likelihood function

$$L = \prod_i [1 + PA(\theta_i, E_i) \cos\phi_i],$$

dropping the factor F_i, since, with respect to P, maximizing W is same as maximizing L. (F_i's being independent of P, the partial derivatives of log L and log W with respect to P are identical.)

The problem of finding the polarization of the recoil protons in K^--p elastic scattering reduces to a search for an azimuthal asymmetry in the subsequent scattering of the protons by a suitable analyzer, or more specifically, obtaining a sample of analyzing powers $A_i \cos\phi_i$ such that P can be estimated through maximizing the likelihood function L.

Technically, it is desirable to set up a simple counter system in such a geometry that $\cos\phi = \pm 1$ (i.e., K^--p and p-C scatterings occur in the same plane) for any θ, so that the comparison of the left-right asymmetry of the p-C scattering leads to a direct estimate of the polarization. Although this technique is convenient for data analysis and does not require an elaborate experimental setup, it is not quite practical for our present purpose because of the relatively weak intensity of K^- beams and the typically small solid angle subtended by the two counters in the double scattering experiment.

In contrast to counter techniques, visual detectors such as emulsion, bubble chamber, and spark chamber can be employed to achieve simultaneously large solid angle and high spatial resolution through their vast detection volume. From the sample of the angular distribution in both θ and ϕ of the proton scatterings and the corresponding analyzability of the scattering medium, the polarization can be estimated by statistical analysis. Of all these detectors, the spark chamber is particularly suitable for this purpose because a counter system for preselecting events can be incorporated. The spark chamber can be placed close to the target in order to minimize the loss corrections for the decay of the short-lived K particles.

In this experiment, a large solid angle and high angular resolution were obtained by surrounding a liquid hydrogen target by a ten-gap cylindrical chamber, followed downstream by a large semicylindrical chamber for the range and polarization information (see Fig. 5).

B. Negative Kaon Beam

Generally, the prime concern in the beam design of particles of finite life is the decrease in the absolute flux during the transport and the increase in the percentage of background particles of longer lives, resulting in larger rejection ratios. Therefore, to use the short-lived beam to maximum efficiency, one has to minimize the distance between the particle source and the detecting system.

As shown in Fig. 2, the magnetic channel used in the experiment consisted of two quadrupole doublet lenses Q_1 and Q_2, and three bending magnets M_1, M_2, and M_3. M_1 was placed as close as possible to the thin window of the west straight section of the Bevatron in order to subtend the largest possible solid angle at the internal target. M_1 and supplementing M_2 bent the negative secondary particles produced in the forward direction by 28 deg and served to define the initial momentum. Q_1 focused the beam at B_1, while Q_2 refocused it vertically at the hydrogen target, and horizontally at infinity. Sandwiched by two spark chambers, M_3 defined the final momentum of the beam before entering the target. With this <u>a posteriori</u> definition of the beam, a large momentum band, $\Delta P/P \approx \pm 5\%$, could be accepted

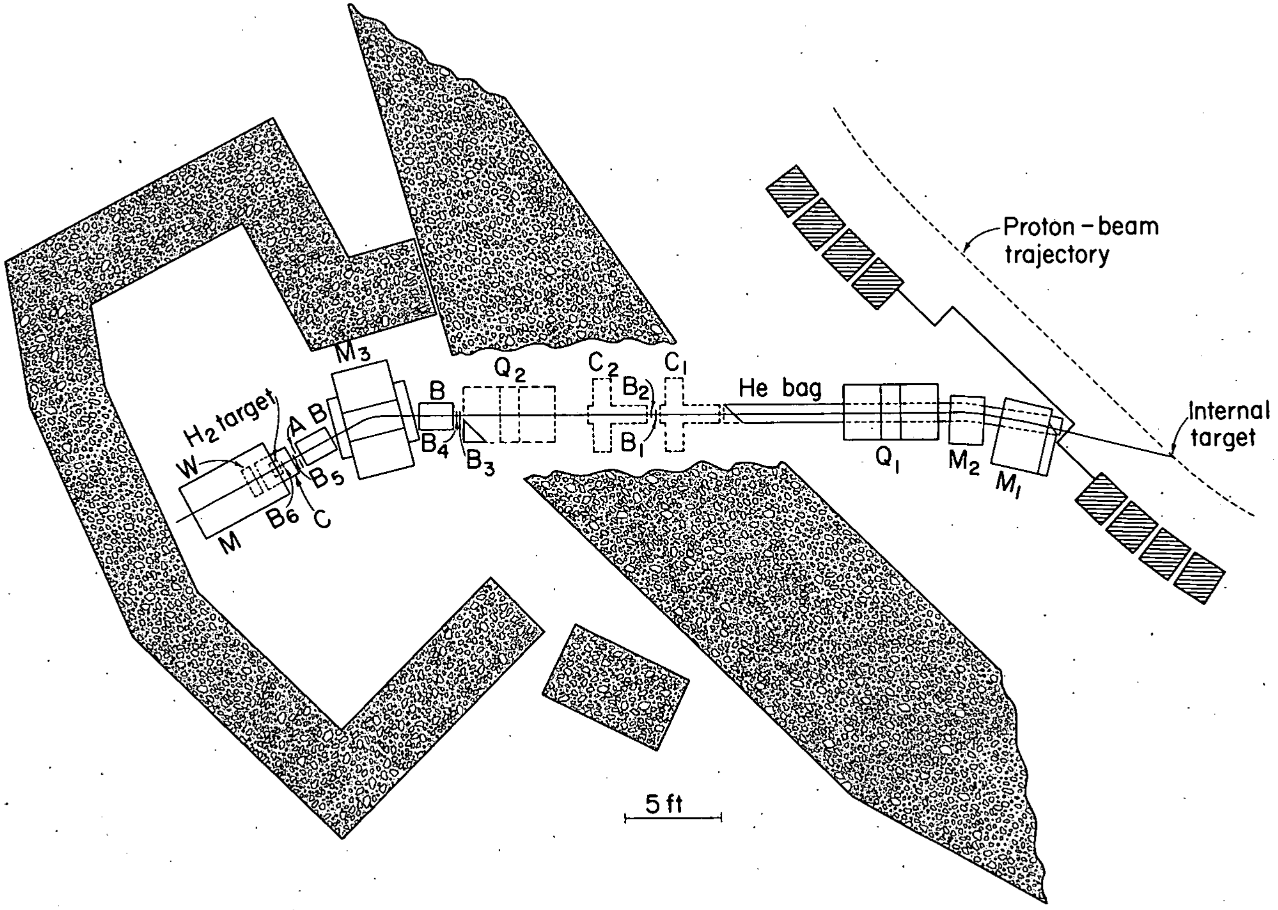

MUB-4337

Fig. 2. Beam layout: M_1 and M_2 are analyzing magnets; Q_1 and Q_2 are quadrupole doublets; B_1 through B_6 and A are scintillation counters; C_1 and C_2 are gas Cerenkov counters; W is a water Cerenkov counter; and B, C, and M are spark chambers.

in order to increase the beam intensity. A helium gas bag was used in part of the beam path in order to reduce beam loss due to the Coulomb scattering and interactions in the air.

To separate the desired K^- beam from the heavy background, six coincident time-of-flight scintillation counters B_1 to B_6 and two anticoincidence high pressure gas Cerenkov counters[14] C_1 and C_2 were employed. (See Section II. D for detailed electronics.) The intensity ratio of π^- to K^- was ≈ 500 with $\approx 10^2$ kaons per 10^{11} circulating protons. The beam pulse length in time was ≈ 300 msec, and a pulse was produced every 6 sec during the experiment.

C. Liquid Hydrogen Target

In order to optimize the effective interaction volume of the hydrogen target and the detection efficiency for low-energy reaction products, particular attention was paid in designing a parallelepiped liquid hydrogen target (Fig. 3). In this way, particles scattered at large angles do not have to traverse so much hydrogen as in the conventional cylindrical target in order to reach the detector, so that the detection efficiency for low-energy particles could effectively be increased.

To achieve this, the almost parallelepiped liquid hydrogen flask was immersed in the hydrogen gas contained in a cylindrical flask whose 0.01-in. Mylar wall isolated the system from the surrounding vacuum. The hydrogen gas was kept in equilibrium with the liquid hydrogen through the four stainless steel pipes (only two are seen in Fig. 3), meeting the boiling-off pipe at joint J; thus the strain on the 0.003-in. Mylar wall of the liquid hydrogen flask was kept at minimum because of the relatively small pressure difference on the two sides of the wall. The weight of the liquid hydrogen was supported by the hydrogen gas feeding pipe, which stretched all the way along the bottom of the flask and joined to the stainless steel end plate. Although the top and bottom of the flask were flat, the beam entrance and exit sides were curved, as is shown in the end view.

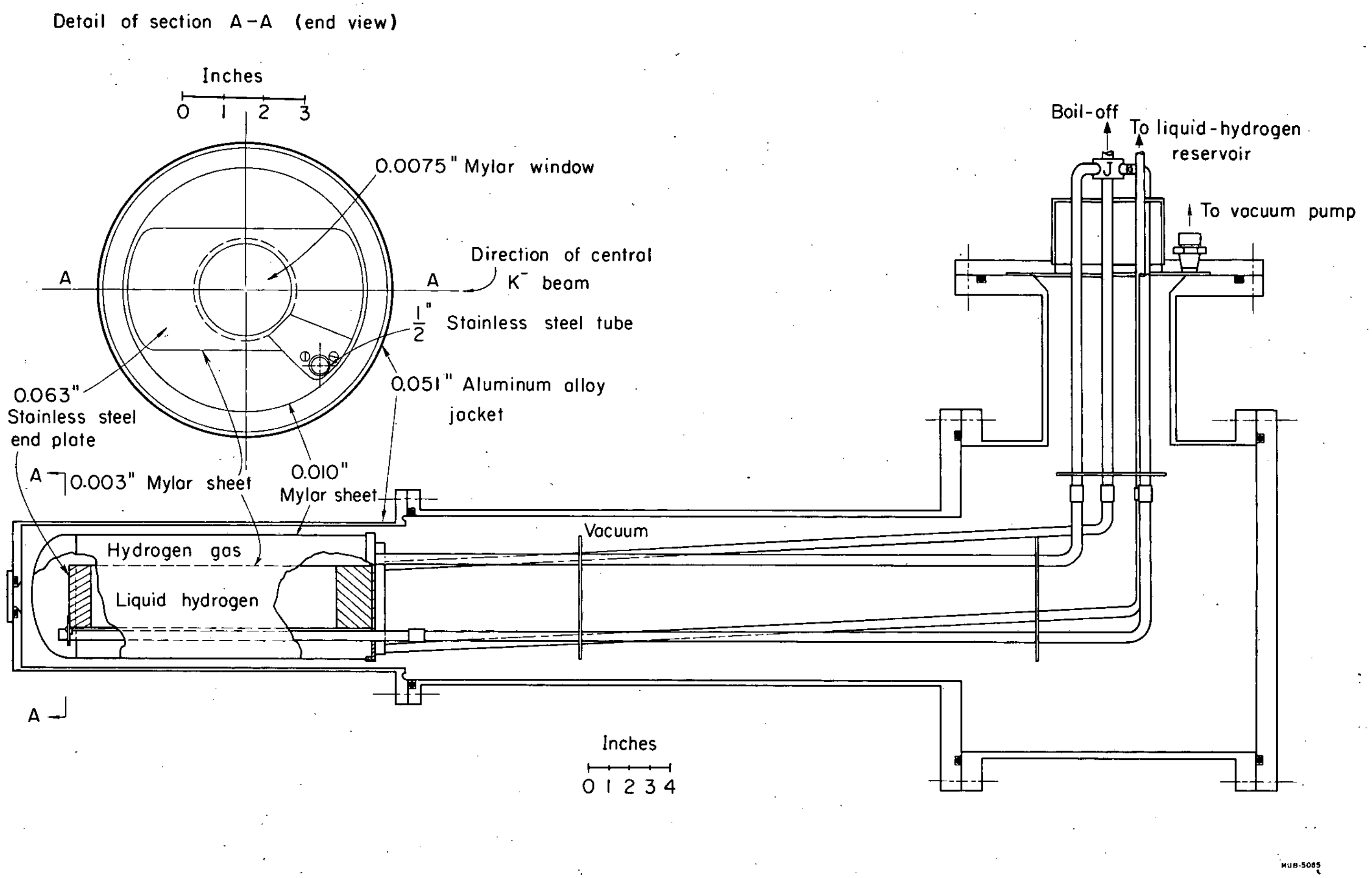

Fig. 3. Details of liquid hydrogen target assembly.

D. Detection

Figure 4 shows the nearly completed setup of the detection apparatus. (The hydrogen target and the cylindrical spark chamber were not yet mounted.) The large semicylindrical chamber is seen at the downstream end. The detailed elevation view is given in Fig. 5. Some details of the detectors have been reported elsewhere.[15]

1. Spark Chambers

A ten-gap cylindrical chamber surrounding the hydrogen target provided a large solid angle and high angular resolution for detecting reaction products. A photograph of the chamber is shown in Fig. 6. The concentric electrodes, 18 in. long and varying in diameter from 10 to 20 in., were made by rolling 0.010-in. aluminum foil into cylinders. They were supported at the ends in circular grooves machined in two polished Lucite end plates. The gap spacing was 0.375 ± 0.010 in. The Lucite post stretching the length of the chamber housed the terminals for electrical and gas connection and also provided a suitable dielectric termination for the straight edges of the electrodes.

A large semicylindrical spark chamber was used to measure the polarization and range of certain reaction products produced in the forward hemisphere. In a big iron frame were contained 21 two-gap chambers, interleaved with absorbers – 12 1-in. carbon absorbers at radii from 18 to 40 in., and 9 0.5-in. curved steel plates extending to a radius of 60 in. The carbon absorbers were made by stacking $32 \times 3 \times 1$-in. graphite bars (density 1.75 g/cm^3) in the slots of the iron frame; the steel absorbers were solid steel plate welded onto the frame. To prevent the straight-through beam from interacting with the absorbers, rectangular openings of sizes ranging from 3×12 in. to 5×12 in. were provided in the middle of each absorber. The transparent curved insulating edge supports for each chamber were made from an annulus of polished Lucite in which three grooves were machined 0.375 in. apart. Electrical connections were made at the bottom edge of each chamber. The whole assembly measured 5 ft wide by 6 ft high by 3 ft deep, and weighed about 6 tons.

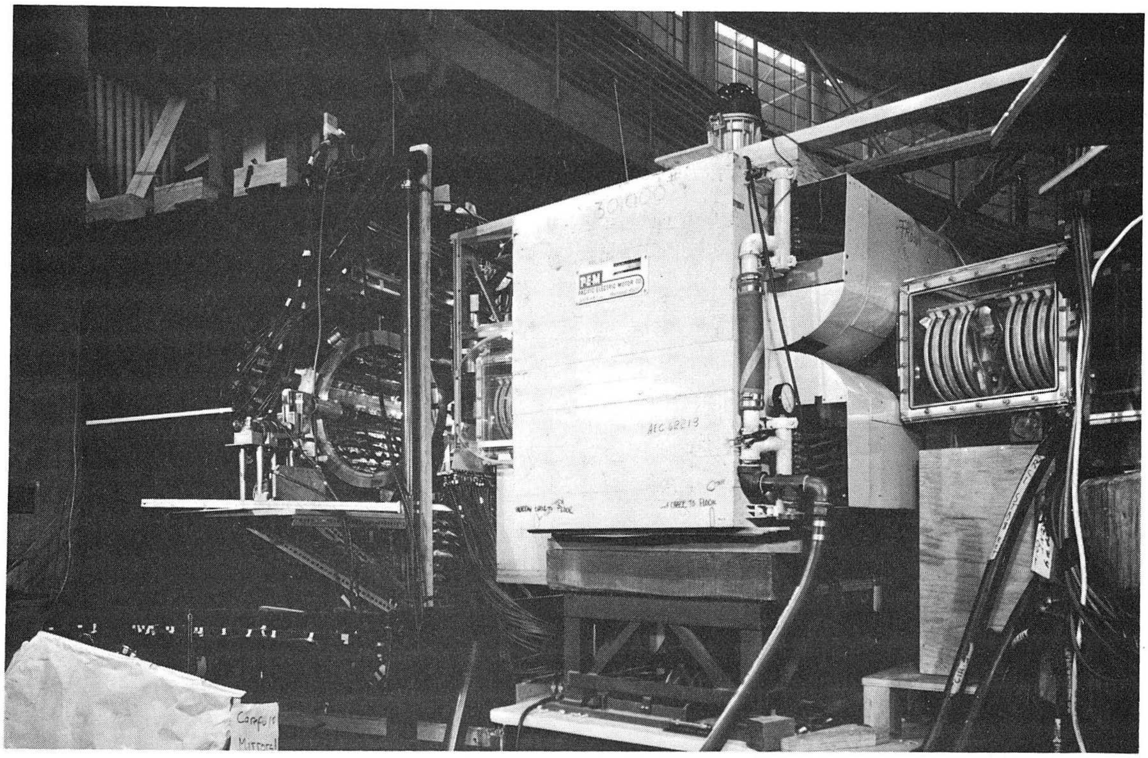

ZN-4894

Fig. 4. View of the nearly completed setup of the detection apparatus. Two momentum-defining chambers are seen on either side of the final analyzing magnet. The large semicylindrical chamber is seen at the downstream end.

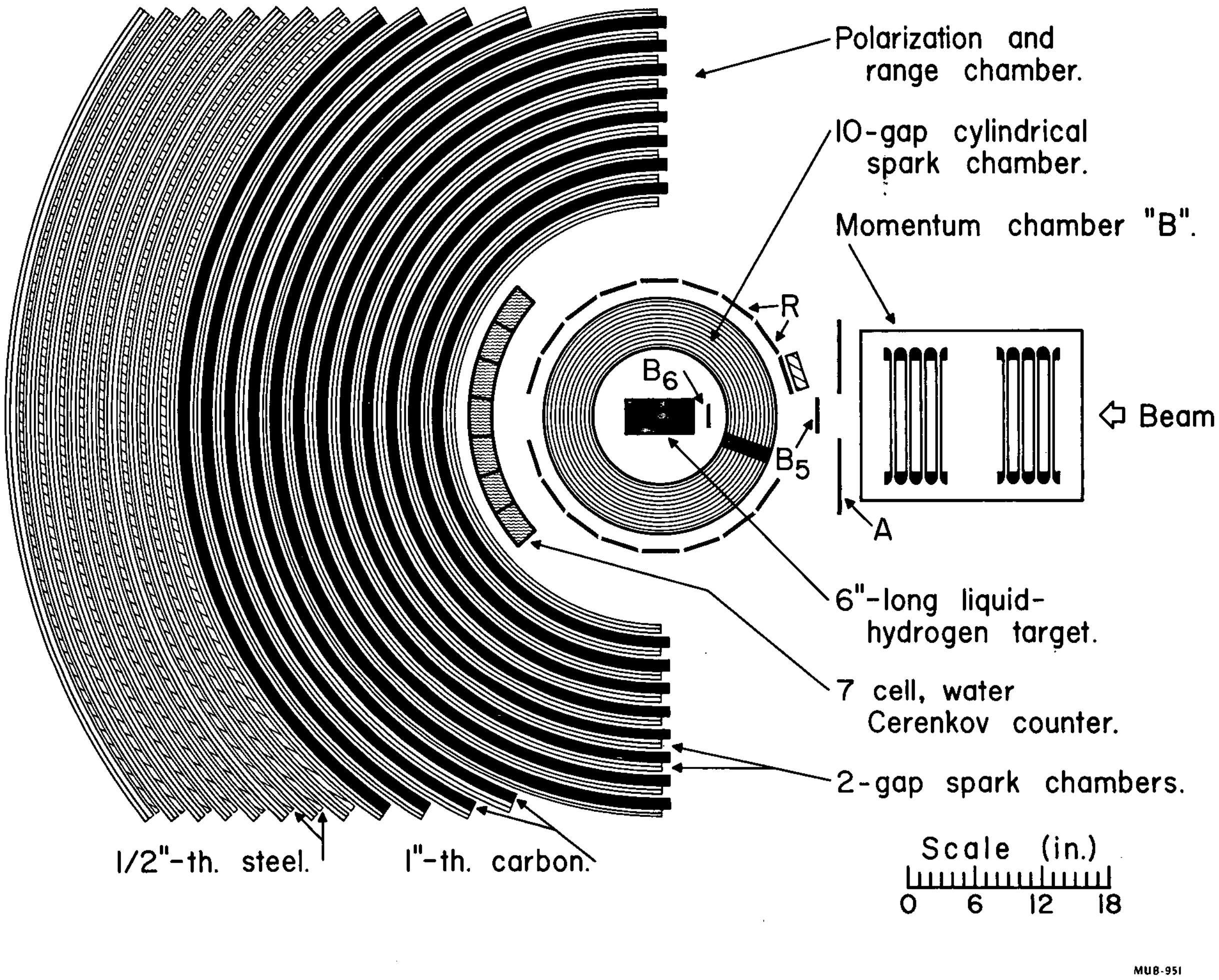

Fig. 5. Elevation view of the apparatus. The upstream momentum-defining chamber and the final bending magnet are not shown.

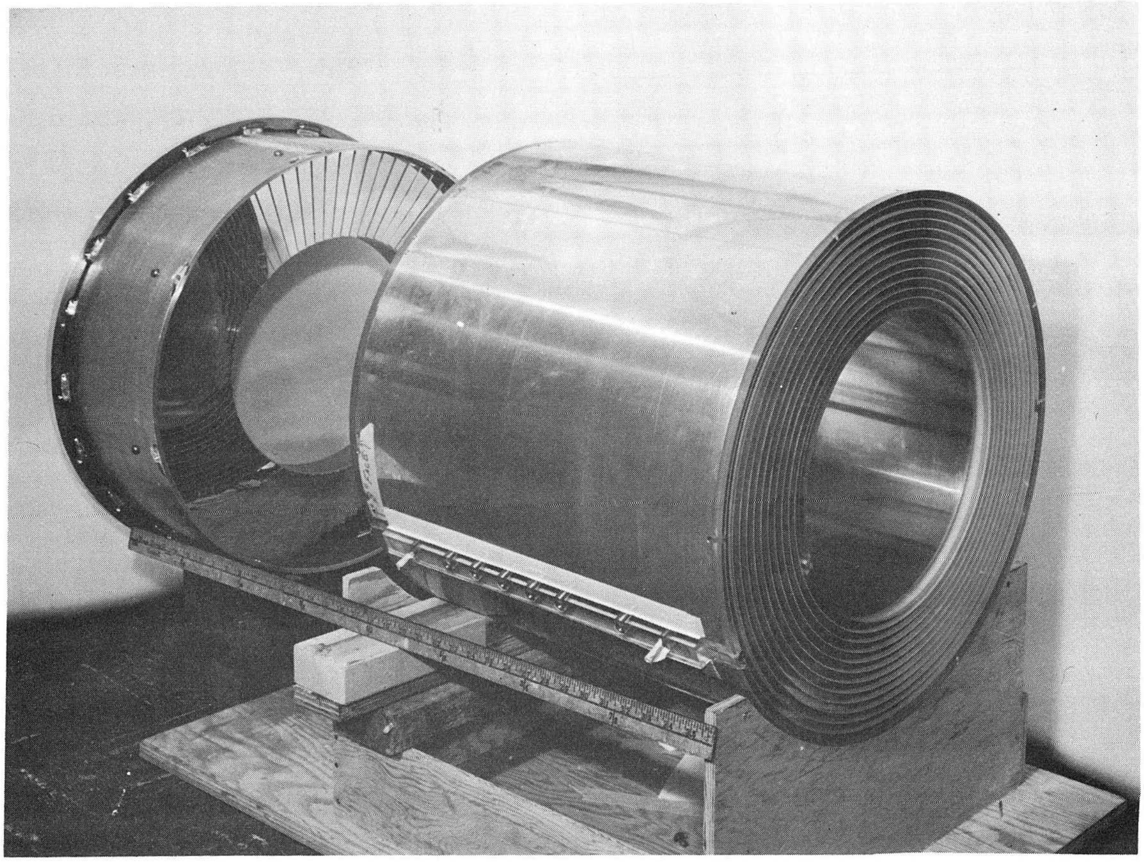

ZN-4895

Fig. 6. Photograph of the cylindrical chamber. The segmented mirror is shown at the left.

The incident momentum of each event could be determined to within ≈ ± 0.5% by means of the precise bending-angle measurement of the tracks recorded by the two beam chambers placed on both sides of the momentum-analyzing magnet. Each chamber consisted of a pair of four 3/8-in. -gap parallel circular plates of 12 in. diameter. They were mounted in an airtight box equipped with two transparent side and top viewing windows. The beam entrance and exit windows as well as the electrode plates were made thin enough (0.003-in. aluminum foils) to minimize the material in the beam path.

To ensure high gas purity and in order to have high detecting efficiency, the chambers were being flushed with a mixture of 90% neon and 10% helium at slightly above atmospheric pressure. To obtain depth and dip-angle information, tilted mirrors were used behind the cylindrical chamber (see Fig. 6) and the range-and-polarization chamber (Fig. 7). The depth Z of a spark from the mirror surface can then be calculated from $Z = d \cot 2\alpha$, where d is the distance between the spark and its image (see Fig. 10) and α is the angle between the normal to the mirror and the axis of the cylindrical electrodes. The mirror segments were arranged on proper backing plates, not exactly radially but almost, in order to increase the visible length of the image for a given cylindrical electrode gap spacing. For the cylindrical chamber $\alpha = 5.7$ deg was used, thus providing a "stereo viewing angle" of 11.4 deg. The α used for the range-and-polarization chamber was 2.85 deg.

2. Counters and Electronics

Details of the counters are given in Table I. Figure 8 shows a simplified diagram for the electronic logic flow.

The α coincidence selected K^- mesons from the beam by means of coincidence of three time-of-flight scintillation counters B_1, B_2, B_5 and an anticoincidence of a high-pressure methane gas Cerenkov counter C_1, which registered only those charged particles with mass smaller than or equal to pions for a given beam momentum. (See also Fig. 2.) The β coincidence functioned similarly to the α

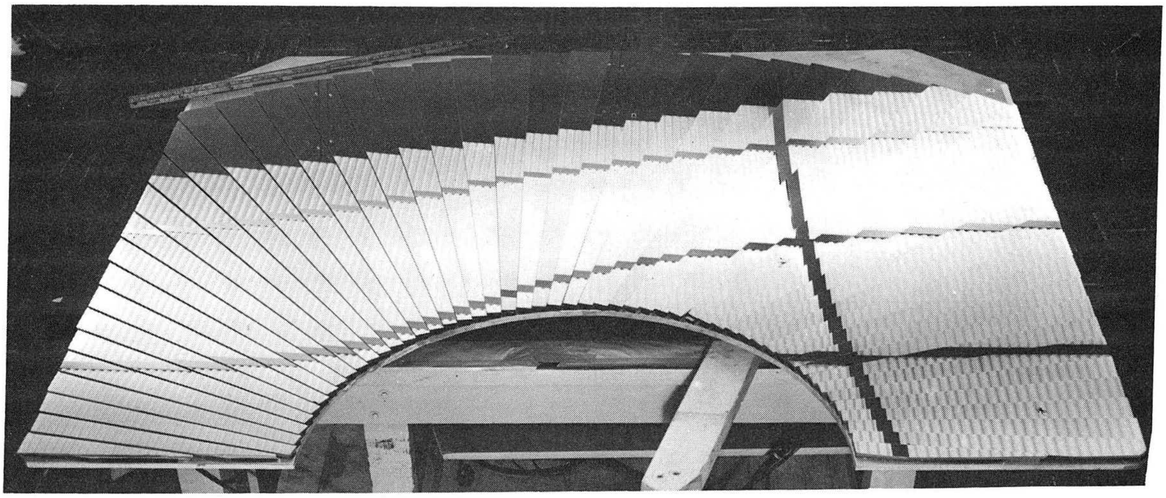

ZN-4896

Fig. 7. Photograph of the segmented mirror for the large semicylindrical chamber.

Table I. Details of counters.

Counter	Type	Dimensions	Function
B_1	Scintillator	2" x 2" x 1/4"	Time-of-flight counters for detecting K^- particles
B_2		2" x 2" x 1/4"	
B_3		6" x 6" x 1/4"	
B_4		6" x 6" x 1/4"	
B_5		8" x 5" x 1/4"	
B_6		8" x 2" x 1/4"	
A	Scintillator	16" x 16" x 1/2" with 8" x 4" rectangular hole	Rejects particles which are out of beam line
C_1	CH_4 Cerenkov	5" diameter	Detect particles lighter than K^--meson for the purpose of anticoincidence
C_2		26" long	
W_0	H_2O Cerenkov	2" x 3 1/4" x 24"	Detect particles with velocity $\beta > 0.75$
W_1			
"			
"			
"			
"			
"			
W_7			
R_1	Scintillator	20" x 3 3/4" x 1/2"	Detect K^--p reaction products
"			
"			
"			
"			
"			
"			
"			
"			
"			
"			
"			
R_{17}			

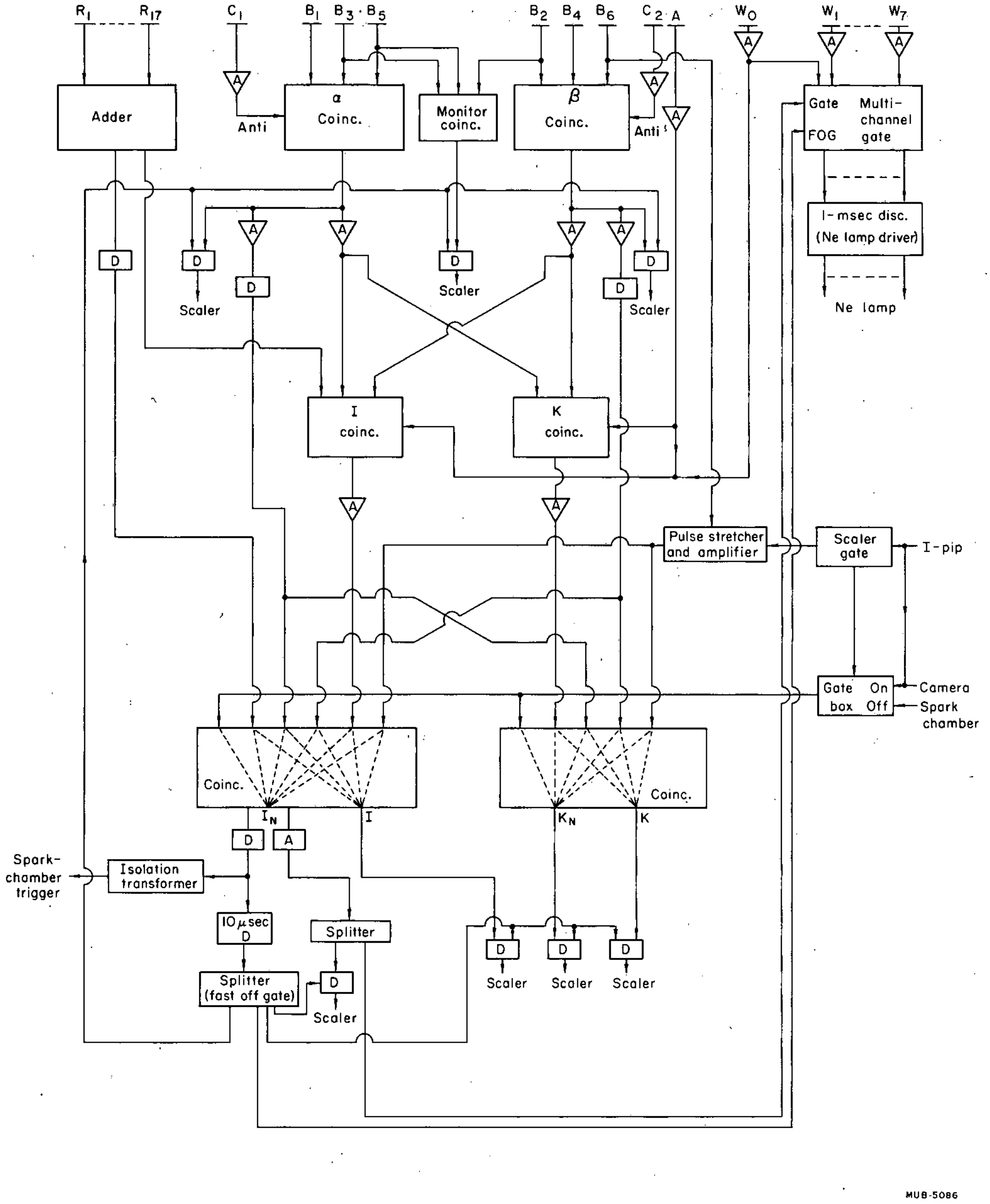

Fig. 8. A simplified diagram for electronics, showing the logic flow used to trigger the spark chambers.

coincidence. To eliminate accidental and spurious coincidences, α and β were again taken in coincidence with counter A in anticoincidence, and formed the K coincidence, which served to identify the desired K^- meson.

The spark chambers were triggered if any two or more of the 17 counters (R_1 to R_{17}) surrounding the cylindrical chamber detected the reaction products of a K^- and a proton (I coincidence circuit of the diagram), provided the camera was ready to take a picture (I_N of the diagram). Eleven triggered spark gaps provided pulses of about -13 kV for the chambers. These gaps were triggered by another spark gap which itself was triggered by a 4PR60 vacuum-tube pulser. The fast-off-gate (FOG) signal derived from the 4PR60 triggering pulse turned off all scalers to prevent them from picking up false counts due to spark noise. A segmented seven-cell water Cerenkov counter (W_1 to W_7; also see Fig. 5) was used to register on the film the charged reaction products with $\beta > 0.75$. A neon lamp indicated the particular cell through which the particle passed.

The total delay between the passage of a particle through the chambers and the start of the high-voltage pulse on the electrodes was about 400 nsec. A clearing field of +35 V (polarity opposite to the high-voltage pulse) was found to achieve the best compromise between high gap efficiency and removal of unwanted background tracks. However, at the beam intensity of about 2×10^5/sec, the background tracks started to appear in a large fraction of the pictures. To obtain clean pictures (i.e., no background tracks), the desired event should not be preceded or followed by a background particle within the sensitive time of the chamber (≈ 0.5 μsec). Accordingly, a long anticoincidence pulse (550 nsec), derived from the beam scintillator B_6 in front of the target, was employed to veto any desirable event preceded by an accidental particle within 0.55 μsec. However, at high beam intensity, the high duty cycle of the long anticoincidence circuit resulted in a suppression of the rate of useful events. No further veto against events with background tracks following the triggering K^- meson was used.

In practice, the maximum rate of accumulation of clean pictures occurred for a flux of 4×10^5 particles per second.

E. Photography

To view all tracks in the various chambers by a single camera, six plano-convex Lucite field lenses of focal length ≈ 29 ft were used: four for the side view of each chamber and two (in conjunction with two 45-deg mirrors) for the top views of the beam chambers. The focal length was limited by the size of the available Lucite plate used to make the lens for the large range-and-polarization chamber. To eliminate spherical abberration, the surfaces of the lenses were made hyperboloidal. Two stages of mirror reflection were needed in order to attain the necessary length of optical path between the spark chambers and the camera. The approximate positions for lenses, mirrors, and the camera, together with the central ray path, are shown in Fig. 9. The camera (Flight Research Model IV) had a recovery time of 38 msec, and therefore was capable of handling up to 10 pictures for a 400-msec beam spill.

Xenon flash lamps, each pulsed by an 8-μF capacitor at 14 kV through a spark gap, were used to illuminate the grids scribed on Lucite plates that were placed behind the field lenses to produce fiducial marks for each chamber. In order to provide a reasonably uniform high-voltage pulse for each chamber and flashing lamp at high pulsing rates, 1400 joules were stored in a capacitor bank recharged between Bevatron pulses. The camera aperture was set at f/15 and Background-X film was used. An example of photograph with rearranged beam chamber picture positions is shown in Fig. 10.

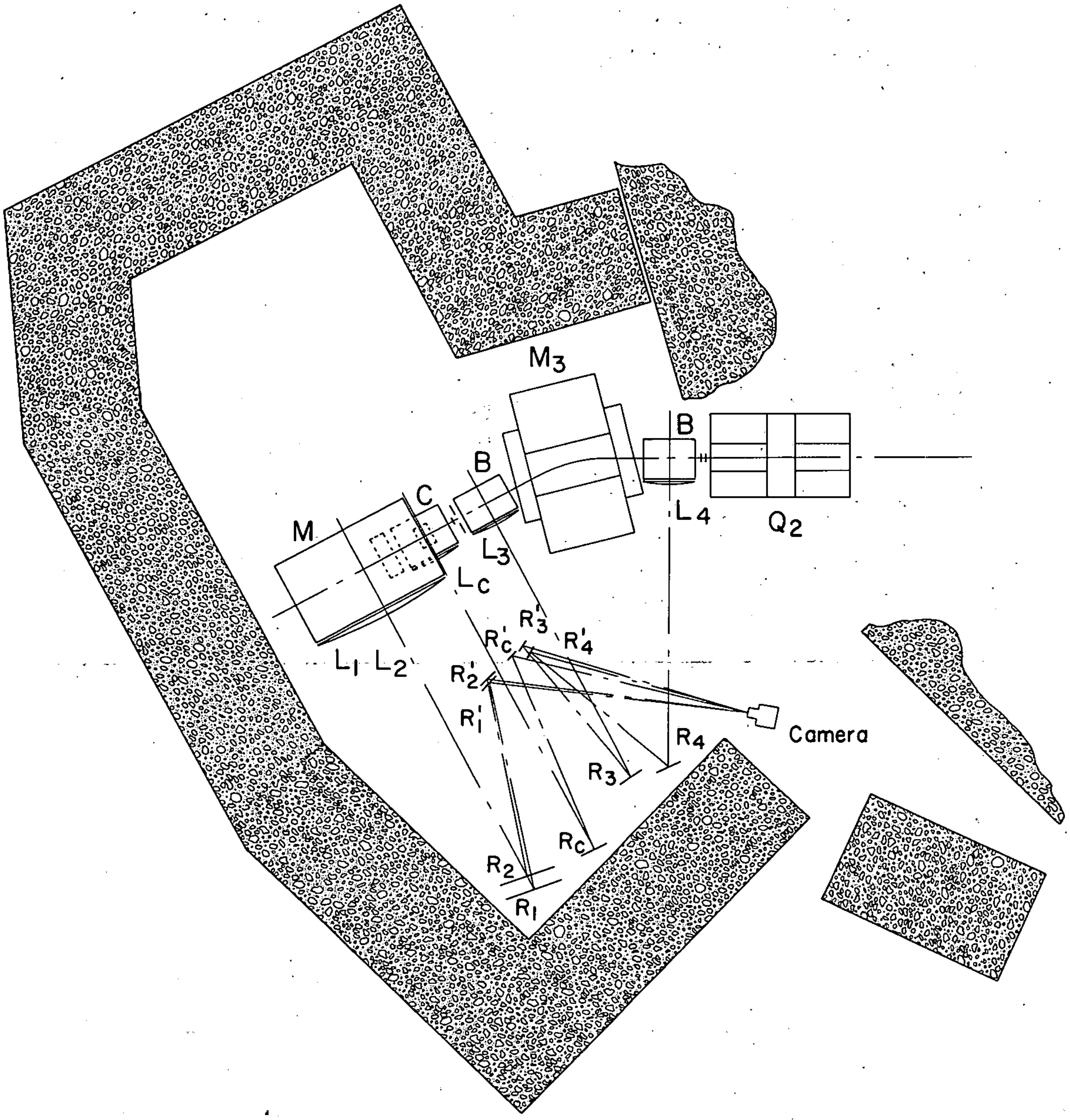

Fig. 9. Spark-chamber optics used to photograph the selected events. Two stages of mirror reflections were used (R_1, R_1', etc.); L_1, L_2, L_c, L_3, and L_4 are field lenses.

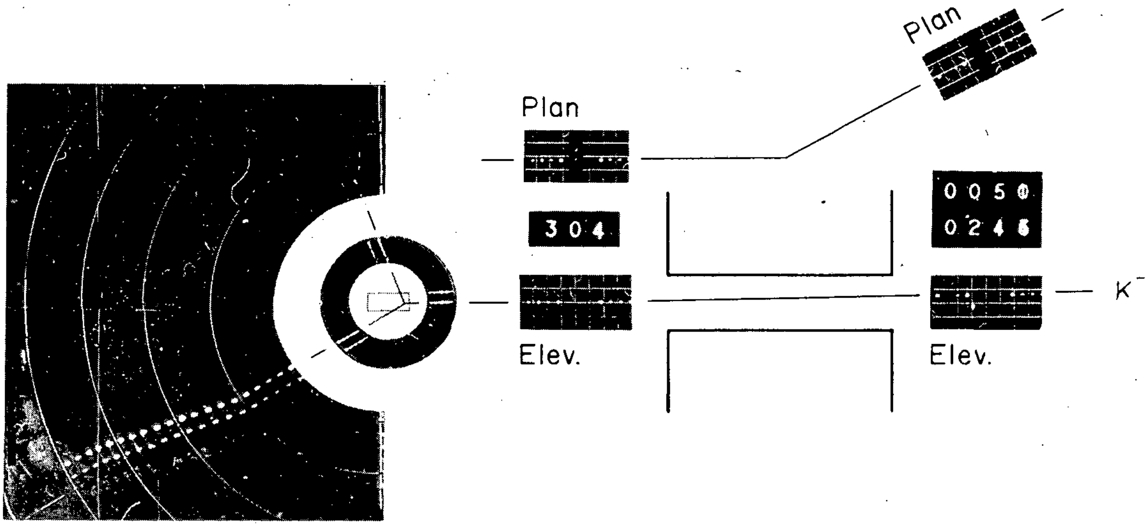

ZN-4897

Fig. 10. Photograph and diagram of an example of K$^-$-p elastic scattering with a subsequent p-C scattering in the polarization and range chamber.

III. DATA ANALYSIS

The major features of the analysis of this experiment can be classified in two categories.

1. Analysis of K^--p elastic scattering: to identify K^--p elastic scattering events by the cylindrical chamber tracks and obtain the elastic differential cross sections.
2. Polarization and phase-shift analysis: to find the polarization of the recoil protons in K^--p elastic scattering by utilizing the p-C scattering in the range-and-polarization chamber, and then make phase-shift analysis by incorporating the elastic differential cross sections. In case of energy-dependent phase-shift analysis other available data such as charge-exchange differential cross sections can also be employed.

Preliminary results of K^--p elastic scattering have been published elsewhere.[16] Final results and the detailed analysis are to be found in Holley's thesis.[4] A simple description of the elastic scattering analysis is given below in order to supplement polarization analysis.

A. K^--p Elastic Scattering: Scanning, Measuring, and Analysis

All the 360 000 pictures taken during the experiment were scanned for three-track events (one incoming and two outgoing tracks). Each track in the cylindrical and beam chambers together with their images and some fiducial lines were measured on SCAMP (Spark Chamber Analyzing and Measuring Projector), a digitized measuring projector developed at this Laboratory for the analysis of photographs from spark chamber events.[17] When the radial fiducial line on the rotatable projection screen is aligned to the projected track of sparks, SCAMP is capable of recording the angle θ and the x-y coordinates of some arbitrary point on the track. These parameters, henceforth called (x, y, θ), are sufficient for constructing a line. Basically what SCAMP does is to record a line in the SCAMP frame of reference.

An IBM 7094 Computer Fortran program, KAPEL, was used to reconstruct the measurement into the spatial tracks. Events were considered elastic when they satisfied kinematical requirements. Each of the two outgoing tracks was assigned to either a proton or kaon according to which assignment fitted the kinematics better (about 6% were found with wrong assignment), and then their kinetic energies were calculated. Also calculated were the incident kaon momentum, K^--p c. m. scattering angle, dip angle of each track, and other relevant quantities. The proton and kaon assignment was then reversed and all calculations were repeated.

B. p-C Scattering

1. Scanning and Measuring

All elastic K^--p scattering events were rescanned, and measurements were made whenever the following criteria were satisfied.

(a) Either one or both of the two outgoing tracks had a scattering in the carbon plates.

(b) The scattering angle in the projected view was greater than 1 deg and smaller than 30 deg. (The lower cutoff angle was later set to 2 deg in the computer program as a compromise between the statistics and scanning efficiency.)

(c) Each scattering had at least two pairs of sparks in a straight line on either side of the vertex in order to ensure a reliable angle measurement.

The measurement of an event consisted of recording the x, y, and θ for some fiducial lines, for the sparks and their images at the entrance to the range-and-polarization chamber, and before and after p-C scattering. Such information was recorded as in which plate the scattering occurred, whether or not the track had further interactions, whether or not the track stopped in the chamber, and if so in which plate it stopped, etc.

Note that at this time no differentiation was made between the two outgoing tracks. This was done for two reasons: firstly, the assignment of proton and kaon for the two tracks by program KAPEL was based on the scattering angles alone, and was therefore sometimes ambiguous (especially when the two scattering angles are close to each other), and secondly, it reduced the load on scanners, who otherwise would have had to make a decision while scanning.

2. Spatial Reconstruction and Kinematical Analysis

For each measured event, the spatial reconstruction and kinematical calculations were done by a second IBM 7094 computer program KAPPOL, incorporating the relevant information provided by the result of KAPEL analysis. The main quantities calculated were:

(a) The continuity parameters. These are the differences at the entrance to the range-and-polarization chamber between the projected angles, dip angles, and x, y, z coordinates of the track concerned, as measured by the track in the range-and-polarization chamber and as expected from extrapolating the track in the cylindrical chamber. These were plotted and proper cutoffs were made in order to exclude events which had scattering in the materials (plastic scintillators, water Cerenkov counters, etc.) between the two chambers.

(b) The azimuthal angle ϕ. This is the angle between the normals of the K^--p scattering plane and p-C scattering plane, namely

$$\cos\phi = \hat{n}_1 \cdot \hat{n}_2,$$

where

$$\hat{n}_1 = \frac{\vec{P}_K \times \vec{P}_P}{|\vec{P}_K \times \vec{P}_P|}, \qquad n_2 = \frac{\vec{P}_P \times \vec{P}'_P}{|\vec{P}_P \times \vec{P}'_P|},$$

and $\vec{P}_K$, $\vec{P}_P$, and $\vec{P}'_P$ are respectively the momenta of the incident kaon, of the recoil proton, and of the proton after scattering off the carbon nucleus. This definition of the sense in $\hat{n}_1$ results in the following convenient sign convention of the proton polarization: A proton recoiling to the right of the incident kaon and scattering again to the right after impinging on the carbon nucleus (i.e., right-right or RR scattering) has the expectation value of the spin parallel to the direction of positive polarization. Similarly, left-left or LL scattering has the same expectation value, while LR and RL scattering have proton spin expectation values parallel to negative polarization.

(c) The kinetic energy of the proton at the p-C scattering, T_p. This was calculated from the energy of the recoiling proton at the K^--p scattering vertex, taking into account the energy losses in the hydrogen target, target walls, scintillation counters, spark chamber plates, water Cerenkov counters, absorbers, etc., up to the point of p-C scattering, which is assumed to be at the center of the carbon plate. The range-energy relations were obtained from the curves of reference 18.

(d) The inelasticity in p-C scattering. The kinetic energy of the proton after scattering off carbon, T_r, was calculated from the residual range by the range-energy relations. The end of each proton track was assumed to be at the center of the final absorber. The distribution of the inelasticity in the p-C scattering, $\Delta E = T_r - T_p$, was plotted for 428 events in Fig. 11. The peak is centered nearly at zero. The half-width on the positive side reflects the energy resolution of the range-and-polarization chamber, which can thus be estimated to be approximately 40 MeV. The large tail on the negative side indicates that a good portion of the p-C scattering went through higher excited states of the carbon nucleus, and the other inelastic processes.

C. Analyzability of Carbon

The curves of constant analyzability for the elastic p-C scattering as a function of laboratory-system momentum and scattering angle were originally given by Birge and Fowler.[19] These curves are not suitable for direct application to polarization measurements, where the energy resolutions of the detecting system are not good enough to distinguish purely elastic p-C scatterings from the inelastic scatterings that go through lower excited states of carbon. The low-lying levels of carbon at 4.43 and 9.6 MeV contribute sizable yields of inelastic scatterings which are polarized essentially the same way as

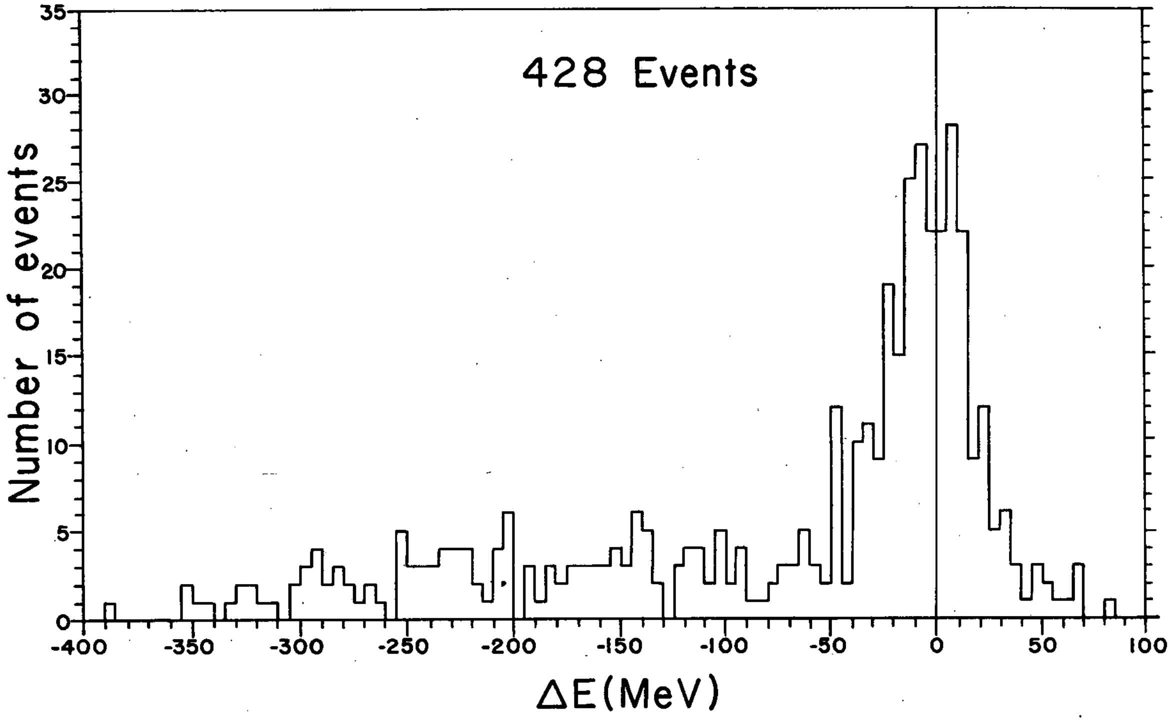

MUB-4968

Fig. 11. The energy distribution of inelasticity in p-C scattering (see text for full description).

elastic scatterings. For higher excited energies, the polarization decreases roughly linearly with the energy loss and becomes essentially zero when more than 30 MeV is lost. Thus a proper analyzability of the carbon should be constructed in accord with the energy resolution of the detecting system. If the energy acceptance of the detector is ΔE, then the average analyzability is given by

$$\bar{A}(\Delta E) = \frac{\sigma_0 P_0 + \int_{E_1}^{\Delta E} \sigma(E') P(E') dE'}{\sigma_0 + \int_{E_1}^{\Delta E} \sigma(E') dE'} ,$$

where P_0 is the polarization in elastic scattering, E_1 is the excitation energy of the first excited state of carbon, and σ_0 and $\sigma(E')$ are the differential cross sections through ground-state and excited-state E', respectively.

Recently, by summarizing the available data, Peterson was able to obtain three sets of analyzability graphs corresponding to $\Delta E = 0$, 30, and 50 MeV.[20] For our present purpose, the last set was adopted in order to match our detector resolution. We also recalculated the polarization, using the graph for $\Delta E = 30$ MeV. It turned out that the estimated polarizations generally decrease in absolute values by small amounts which are unimportant in view of the large statistical errors. The graph for $\Delta E = 50$ MeV is reproduced in Fig. A-1 of Appendix A. More recently, analyzability including all inelastic p-C scatterings became available at higher energies.[21] It is given in Table A-I of Appendix A.

To obtain analyzabilities for our sample scatterings, data from Fig. A-1 and Table A-I were stored in the computer memory, and proper interpolation was made. Though Fig. A-1 provides analyzability up to 375 MeV, values from Table A-I were used for proton energies greater than 325 MeV. This was so done in order to secure a smooth connection between the two independent sets of data.

D. Selection Procedure and Estimation of Polarization

1. Selection Procedure

Of about 15 000 K^--p elastic scatterings, measurements were made for ≈ 6000 events found to have the scattering in either one or both of the two outgoing tracks. Although assignment of a proton or kaon to either track was done by the program KAPEL, this information was momentarily suppressed, and any track that had a scattering in a carbon plate was assumed to be a proton. In case both tracks had scattered in carbon plates, one was first assumed to be a proton. After all calculations had been done, the assignment was reversed. Selection was made by the continuity parameters discussed in Section B; however, events with proton energy T_p less than 325 MeV but inelasticity ΔE greater than 50 MeV were also rejected. In total, 1535 events were found with useful analyzing power. These events were then checked carefully with the photographs, and final decision of proton assignment was made by utilizing all information available, such as residual range and the particle velocity information provided by water Cerenkov counters, in addition to the kinematical fitting of KAPEL. About two-thirds of the above events (1058 to be exact) turned out to be K^--C scatterings.

The useful p-C scattering samples so obtained were treated by the maximum-likelihood method for polarization estimation. Details of this method are given in the following section. The cutoff angle in the projected view was set to be 2 deg. The polarization was found not very sensitive to the cutoff angle. This is because the events with small scattering angle generally have very small analyzing powers. A total of 477 events throughout the whole momentum region was finally accepted. These events were divided into five groups according to the incident kaon momentum. The momentum intervals were chosen to cover the regions of interest without making the statistics unreasonably poor. These momentum intervals seem to display a most marked variation of polarization as a function of momentum. Polarization is, of course, generally a function of momentum; it is, however, assumed constant within a given momentum interval.

2. Estimation of Polarization

With the analyzing-power samples $A_i \cos \phi_i$ on hand, we are ready to estimate the polarization by the likelihood function described in Section II. A, namely,

$$L (P) = \prod_i (1 + PA_i \cos \phi_i).$$

It is known that P can be expanded in the cosine series:

$$P = \frac{\sin \theta}{\sigma (\theta)} \sum_{n=1}^{2\ell-1} \cos^n \theta,$$

where $\sigma (\theta)$ is the K^--p elastic differential cross section, θ is the c.m. scattering angle, and ℓ is the highest partial wave involved.

Approximation 1. P is assumed constant within small angular interval

Apparently P is a function of θ. It is, however, a common practice to treat P as a constant within a small range of cos θ, so that it can be estimated by maximizing L with respect to P. The computation was done by the IBM 7094 and the result was plotted by the CAL-COMP plotter. Examples of four typical shapes of L are shown in Fig. 12. Figure 12-A and -B show near Gaussian distribution of L with the peak inside the physical limit ($-1 \leq P \leq 1$). Figure 12-A has a reasonable number of events while Fig. 12-B is statistically poor. The statistical error may be defined as that increment of P that makes L/L_{max} equal to $e^{-1/2}$ in accord with one standard deviation interpretation of likelihood interval (i. e., 68% confidence interval of likelihood function). Figure 12-C and -D show the case in which the peak of L lies outside the physical region. This behavior is possible because of the functional characteristics of the polynomial L. In the limiting case in which the analyzing powers $A_i \cos \phi_i$ are all of the same sign, L becomes a monotonically increasing or decreasing function. In

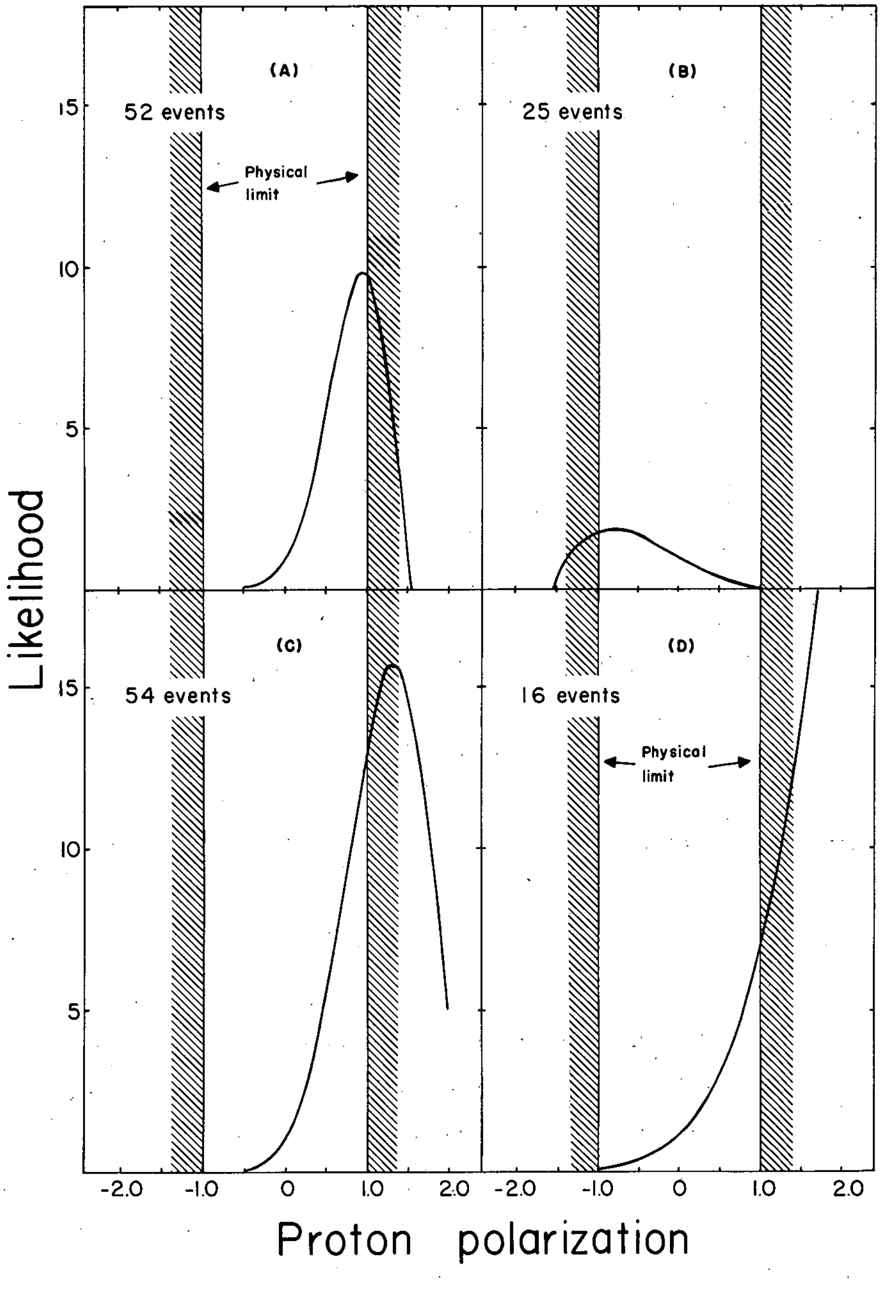

MUB-4975

Fig. 12. Examples of four typical shapes of the likelihood function L(p).

Fig. 12-C, one can still infer the polarization as $P = 1.32 \pm 0.54$, and use this value in further studies, such as phase-shift analysis. For Fig. 12-D, however, we are obliged to assign the polarization as $1.0 \pm \Delta P$, where ΔP is arbitrarily defined as the increment of P which renders $L/L(P = 1)$ equal to $e^{-1/2}$. (See, e.g., Fig. 17. Arrows in the error bars indicate that the likelihood functions diverge in that direction.)

Whether or not the polarization is reasonably constant within the given angular bin can be tested by two means. Firstly, one can try several different angular bins and compare the results. This serves to explore the general behavior of polarization as a function of $\cos\theta$. Secondly, one can observe the behavior of the likelihood function as a function of the size of the angular bin. A decrease in the likelihood function despite the increase in statistics obtained by enlarging the size of angular bin means that the polarization is changing rather rapidly in the enlarged region of the angular bin, hence it is a poor approximation to treat the polarization as a constant in the whole angular interval.

The final selection of angular bins was made with the best compromise between the statistics and the constancy of the polarization. The results are given in Table II and are plotted in Figs. 13-B through 17-B. In the graphs (A) are plotted the sums of positive and of negative analyzing powers respectively in the given angular bins. This corresponds to counting up the total effective analyzing power of opposite signs in these intervals. The ordinate can therefore be interpreted as the "equivalent number of right vs left scatterings of unit analyzing power," or it might also be thought of as the number of events that an equivalent counter experiment (of such geometry that $\cos\phi_i = 1$ and $A_i \approx 1$) might have recorded.

Approximation 2. Linear approximation

A natural extension of the constant approximation is made by assuming the polarization to be a linear function of $\cos\theta$ within certain angular interval. Thus if one writes

$$P = c\,(1 + b\cos\theta),$$

Table II. Polarization of recoil protons in K^--P scattering.

Incident K^- momentum (MeV/c)	Cos θ^*	Polarization
817^{+83}_{-89}	$-0.779^{+0.170}_{-0.197}$	$0.92^{+0.36}_{-0.40}$
798^{+90}_{-89}	$-0.467^{+0.180}_{-0.132}$	$-0.78^{+0.68}_{-0.54}$
850^{+47}_{-95}	$-0.008^{+0.334}_{-0.186}$	$-1.10^{+0.63}_{-0.54}$
953^{+47}_{-49}	$-0.809^{+0.159}_{-0.133}$	$1.32^{+0.48}_{-0.54}$
944^{+53}_{-42}	$-0.442^{+0.204}_{-0.208}$	$-0.40^{+0.56}_{-0.52}$
960^{+39}_{-57}	$0.010^{+0.321}_{-0.177}$	$-1.12^{+0.83}_{-0.72}$
1052^{+48}_{-51}	$-0.849^{+0.090}_{-0.125}$	$1.42^{+0.86}_{-0.86}$
1044^{+50}_{-43}	$-0.648^{+0.143}_{-0.100}$	$0.04^{+0.80}_{-0.73}$
1053^{+42}_{-48}	$-0.255^{+0.252}_{-0.231}$	$-0.96^{+0.64}_{-0.56}$
1057^{+36}_{-51}	$0.214^{+0.225}_{-0.212}$	$-0.66^{+1.10}_{-0.82}$
1146^{+52}_{-45}	$-0.714^{+0.209}_{-0.209}$	$-1.16^{+0.73}_{-0.71}$
1147^{+53}_{-45}	$-0.334^{+0.306}_{-0.163}$	$0.66^{+0.85}_{-0.89}$
1160^{+35}_{-58}	$0.320^{+0.168}_{-0.315}$	$-1.04^{+0.84}_{-0.71}$
1267^{+54}_{-46}	$-0.785^{+0.057}_{-0.074}$	$1.0^{+0.29}_{-0.29}$
1269^{+70}_{-66}	$-0.559^{+0.155}_{-0.118}$	$1.0^{+0.62}_{-0.62}$
1253^{+68}_{-48}	$-0.182^{+0.178}_{-0.148}$	$1.0^{+0.55}_{-0.54}$
1275^{+87}_{-69}	$0.342^{+0.242}_{-0.320}$	$-1.0^{+0.44}_{-0.44}$

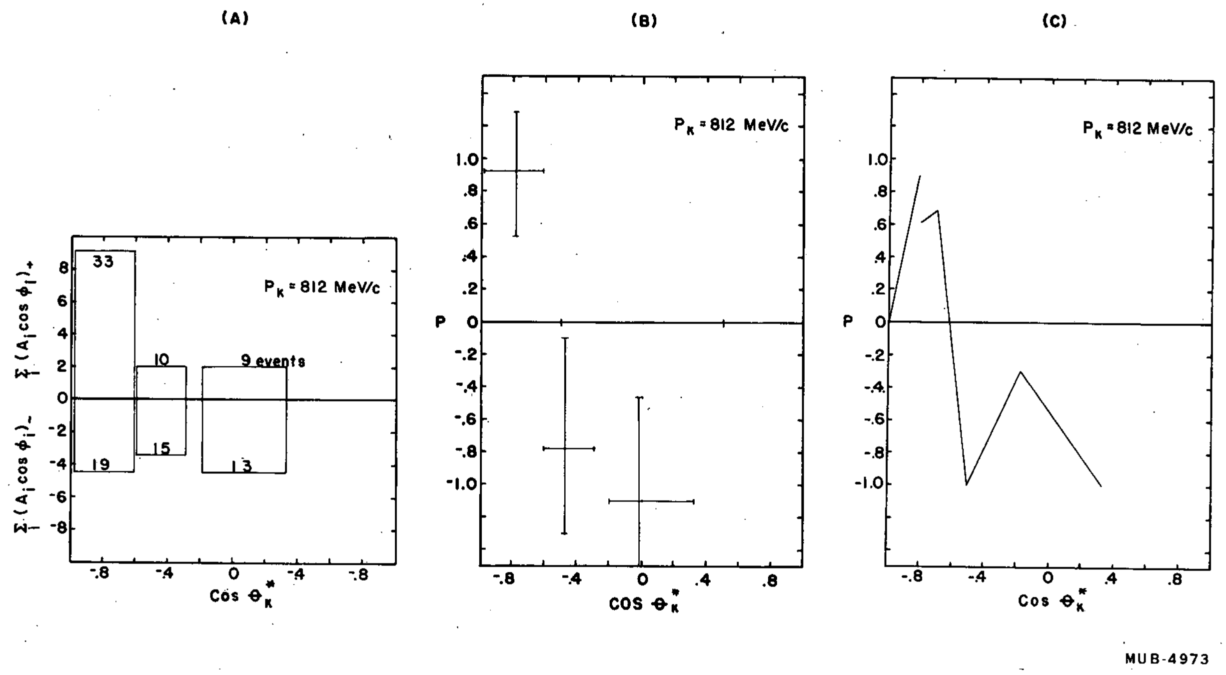

Fig. 13. (A) Sums of positive and of negative analyzing powers respectively in given angular regions.

(B) The angular distribution of the polarization. (The polarization is assumed to be constant within the given angular region.)

(C) The angular distribution of the polarization. (The polarization is assumed to be a linear function within the given angular region.)

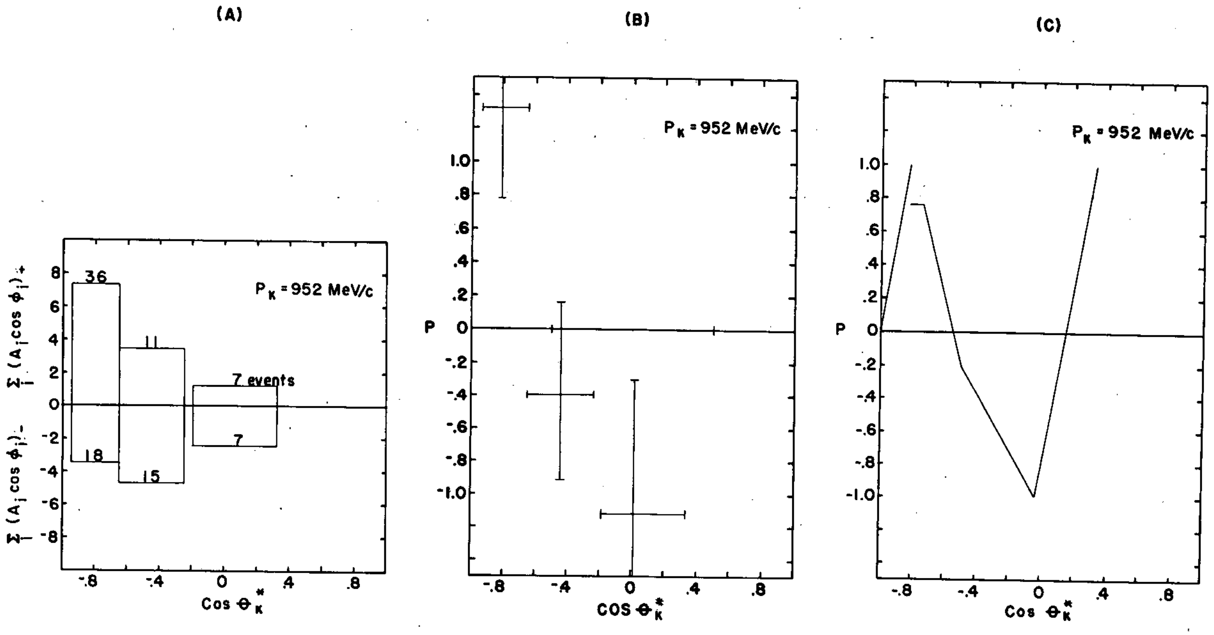

MUB-4972

Fig 14. (A) Sums of positive and of negative analyzing powers respectively in given angular regions.

(B) The angular distribution of the polarization. (The polarization is assumed to be constant within the given angular region.)

(C) The angular distribution of the polarization. (The polarization is assumed to be a linear function within the given angular region.)

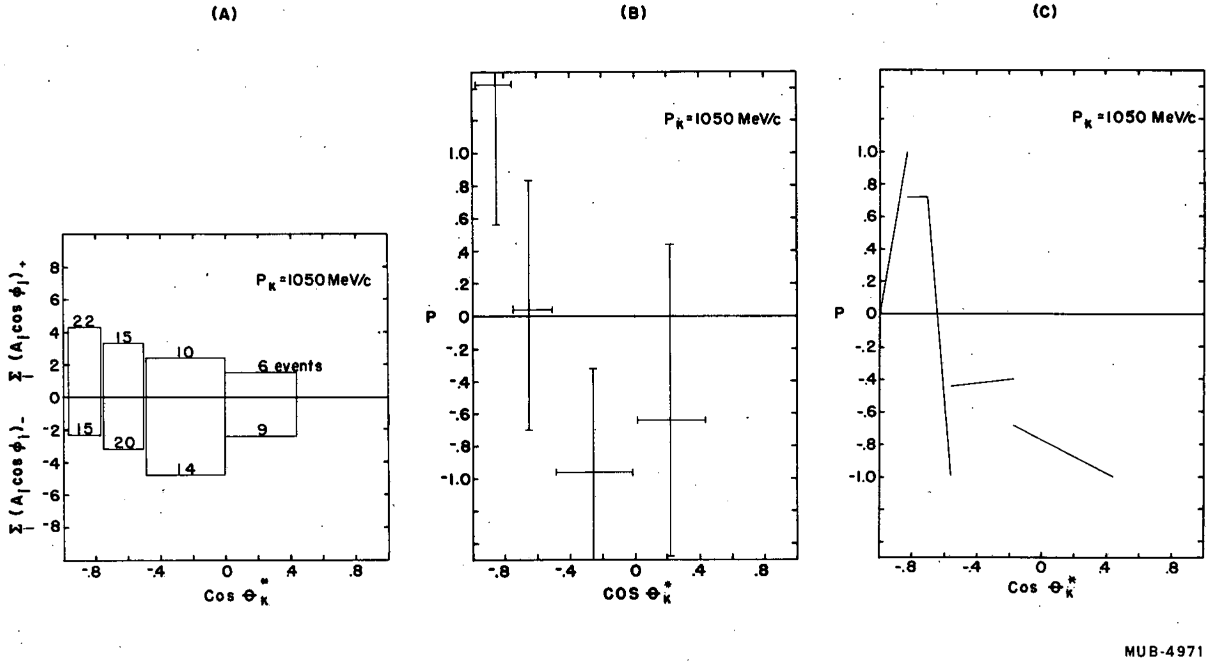

Fig. 15. (A) Sums of positive and of negative analyzing powers respectively in given angular regions.

(B) The angular distribution of the polarization. (The polarization is assumed to be constant within the given angular region.)

(C) The angular distribution of the polarization. (The polarization is assumed to be a linear function within the given angular region.)

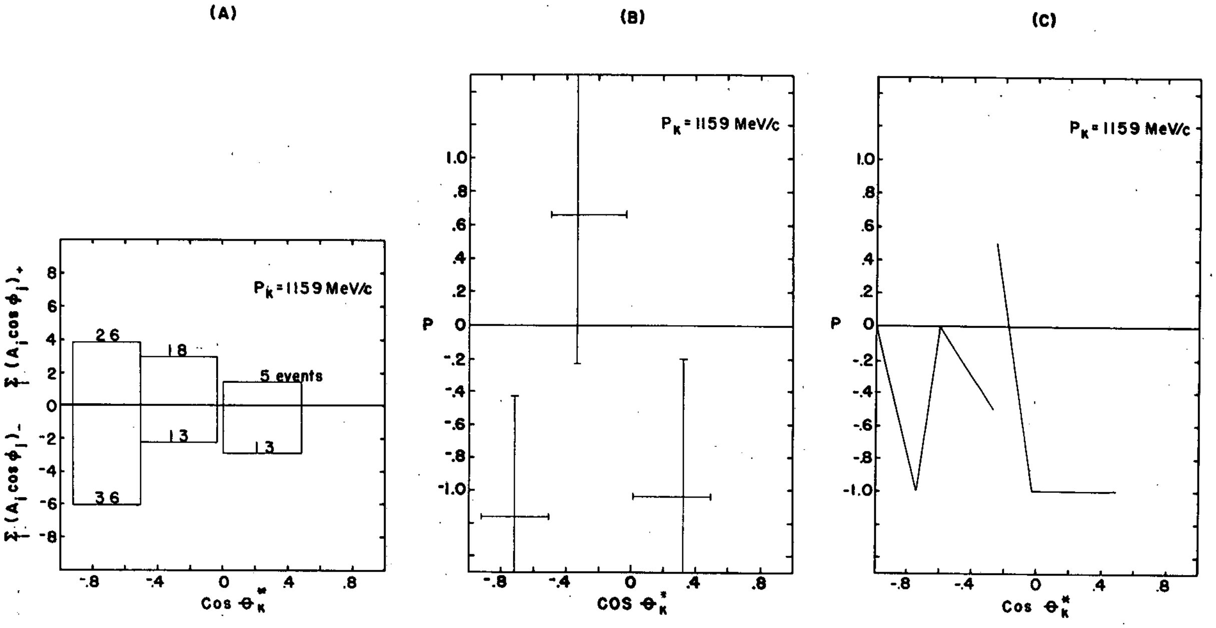

MUB-4970

Fig. 16. (A) Sums of positive and of negative analyzing powers respectively in given angular regions.

(B) The angular distribution of the polarization. (The polarization is assumed to be constant within the given angular region.)

(C) The angular distribution of the polarization. (The polarization is assumed to be a linear function within the given angular region.)

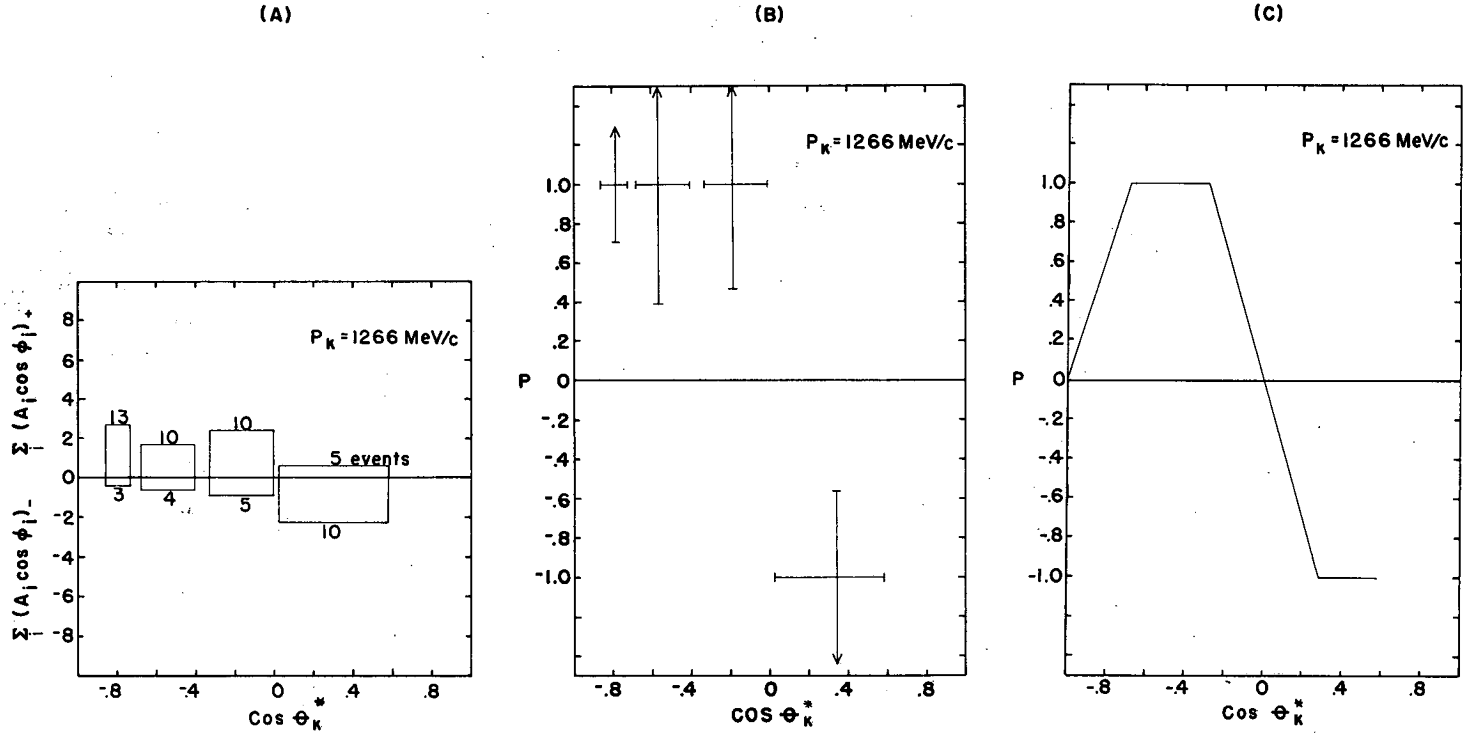

MUB-4969

Fig. 17. (A) Sums of positive and of negative analyzing powers respectively in given angular regions.

(B) The angular distribution of the polarization. (The polarization is assumed to be constant within the given angular region.)

(C) The angular distribution of the polarization. (The polarization is assumed to be a linear function within the given angular region.)

L can be maximized (L_{max}) by varying c while keeping b constant. Several values of b can be chosen and corresponding L_{max}'s are compared. It is important to start from the angular bin that possesses the boundary condition of vanishing polarization at one end ($P = 0$ at $\cos\theta = \pm 1$). The best compromise between the bin size and the statistics allows the best estimation of the polarization as a function of $\cos\theta$. In our case we chose ≈ 20 samples of analyzing powers ($A_i \cos\phi_i$, $i = 1$ to ≈ 20). After the best linear approximation is obtained, the value of the polarization at the end of this interval can then be used as the starting point of the next angular bin. In this way, the polarization can be represented by a set of line segments. The result is shown in Figs. 13-C through 17-C. The variation of P as a function of $\cos\theta$ can be used to double-check the suitability of the $\cos\theta$ intervals selected in the constant approximation of the preceding section.

It is apparent that the linear approximation is more general than the constant approximation, since the former reduces to the latter when b vanishes. That the former is a better approximation than the latter is assured by the higher amplitude of the likelihood function obtained for given samples of $A_i \cos\phi_i$ (see Appendix B). Whereas this is the merit of linear approximation, this method has a difficulty in error assignment. If the error is given by $\Delta P = \Delta c\,(1 + b\cos\theta)$, where Δc is that increment of c for which $L/L_{max} = e^{-1/2}$, as is defined for the constant approximation, then ΔP becomes a function of $\cos\theta$. When plotted, it gives an "error band" of varying width. (See Fig. B-1-B of Appendix B.)

E. Uncertainties, Errors, and Reproducibility

In light of the large statistical uncertainty in the estimated polarization, the correction needed for errors due to other uncertainties turned out to be relatively unimportant. Some factors that may contribute to the uncertainties are the following:

1. Scanning Efficiency

The scanning efficiency for the K^--p elastic scattering was about 85%, and the efficiency of the double scan for p-C scattering was estimated to be greater than 97%. The scanning efficiencies for left and right scatterings are believed to be the same. Hence the difference in the scanning efficiency from 100% merely reduces the confidence in the value of scattering asymmetry through the increased statistical uncertainty due to the decrease of the number of events detected.

2. p-Al Scattering Contamination

The spatial resolution of the range-and-polarization chamber sparks did not allow the p-C scattering to be distinguishable from p-Al scattering when this occurred in the aluminum electrodes next to the carbon absorbers. They were all treated as p-C scattering, because this contamination is believed to be small owing to the relative thickness of carbon and aluminum plates; besides, aluminum has analyzability fairly comparable to that of carbon, except for inelastic scatterings.[22]

3. Accuracy of Measurement

The measuring projector, SCAMP, is capable of recording the (x, y, θ) coordinate of a line to an accuracy of 1 micron in x, y and 0.628 mrad in θ. The major error in the measurement was introduced in aligning the fiducial line of the projection screen with the rather wide sparks. This error is most seriously propagated in the calculation of the depth of the sparks, since the resolution in depth is only about 1/5 as good as the resolution of the direct view for the cylindrical chamber, and only 1/10 as good for the range-and-polarization chamber.

The overall effect of the accuracy of measurement on the estimated polarization was checked by remeasuring about one-third of the accepted events. All quantities, including the p-C scattering angle, azimuthal angle between the p-C and the K^--p scattering planes, analyzability, etc., were compared for the two measurements. They were found to be in fair agreement.

IV. PHASE-SHIFT ANALYSIS

A. Single-Energy Phase-Shift Analysis

Analysis of the elementary particle scattering in terms of partial-wave phase shifts has been very successful in interpreting the π^+p (3, 3) resonance,[23] and has since been applied extensively in π-N scattering. Aside from the different isotopic spin decomposition in scattering amplitudes, the formalism is identical for the K-N system, since they both involve interactions between spin-0 and spin-1/2 particles.

In this formalism, polarization, differential cross section, and total cross section at each energy can be fitted in terms of phase shifts $\delta_{\ell\pm}$ and absorption parameters $\eta_{\ell\pm}$, where $\ell\pm$ stands for $\ell \pm 1/2$. They are related to the partial-wave scattering amplitude $A_{\ell\pm}$ by

$$A_{\ell\pm} = \frac{e^{i\,2\,\rho_{\ell\pm}} - 1}{2\,i}\,, \tag{1}$$

where

$$\rho_{\ell\pm} = \delta_{\ell\pm} + i\,a_{\ell\pm} \tag{2}$$

is the complex phase shift, and the absorption parameter is defined by

$$\eta_{\ell\pm} = \exp(-2a_{\ell\pm}) \tag{3}$$

The spin-flip and spin-non-flip amplitudes are given respectively by

$$f(\theta) = \lambda\!\!\!\!\sum_{\ell=0}^{\ell_m} [(\ell + 1)\,A_{\ell+} + \ell\,A_{\ell-}]\,P_\ell\,(\cos\theta) \tag{4}$$

and

$$g(\theta) = \lambda\!\!\!\!\sum_{\ell=0}^{\ell_m} [A_{\ell-} - A_{\ell+}]\,\sin\theta\,\frac{d}{d\,(\cos\theta)}\,P_\ell\,(\cos\theta), \tag{5}$$

where λ is the kaon wave number and θ is the scattering angle in the c.m. system, P_ℓ is the lth-order Legendre polynomial, and ℓ_m is the highest partial wave involved. Finally, through Eqs. (1) through (5), the phase shifts and absorption parameters are related to the experimental observables, namely differential cross section, polarization and the total cross section, respectively, by

$$\frac{d\sigma}{d\Omega} = |f|^2 + |g|^2, \tag{6}$$

$$P = \frac{2\, I_m\, f^* g}{d\sigma/d\Omega}, \tag{7}$$

and

$$\sigma_T = 4\pi \bar{\lambda}\, I_m\, f(0) \quad \text{(optical theorem)}, \tag{8}$$

where $I_m\, f(0)$ is the imaginary part of the forward scattering amplitude for k-N elastic scattering.

KAPANAL, written originally by Foote[24] as PIPANAL for π^+-p scattering, and later modified by Cook[25] for the K^+-p system, is a least-square grid search program which, starting from a set of random numbers generated in the intervals $0 < \delta < 180$ deg and $0 < \eta \leqslant 1.0$, finds a set of phase shifts and absorption parameters that best fit the experimental data, or minimize the χ^2:

$$\chi^2 = \sum \left\{ \left| \frac{\frac{d\sigma}{d\Omega}^c - (1+\epsilon)\frac{d\sigma}{d\Omega}^e}{\Delta \frac{d\sigma}{d\Omega}^e} \right|^2 + \left| \frac{\epsilon}{\Delta\epsilon} \right|^2 + \left| \frac{P^c - P^e}{\Delta P^e} \right|^2 + \left| \frac{\sigma_T^c - \sigma_T^e}{\Delta \sigma_T^e} \right|^2 \right\}, \tag{9}$$

where the superscripts c and e represent the calculated and experimental values of the data points, ϵ is the normalization parameter for the differential cross section, and Δ indicates the uncertainties in the relevant quantities. The summation is over all experimental quantities being considered. As soon as the minimum χ^2 for a given set of phase shifts is reached, the search can be repeated with a new set of random numbers, thus eventually covering most of the χ^2 surface. One hundred trials were made at each momentum.

Since KAPANAL was written for the K^+-p system (which is a pure isotopic spin $T = 1$ state), when it is applied to the K^--p scattering (a mixed state of T = 1 and 0) the resulting phase shift δ is a lumped phase shift of δ_0 and δ_1. (Here and henceforth the subscripts refer to the I-spin state.) With the use of Clebsch-Gordan coefficients, the K^--p system can be written as a sum of two different $|T, T_3\rangle$ states as

$$|K^-p\rangle = \frac{1}{\sqrt{2}}\left\{|1,0\rangle + |0,0\rangle\right\}. \tag{10}$$

Hence the scattering amplitude becomes

$$A = \frac{1}{2}(A_1 + A_0). \tag{11}$$

Making use of

$A = (\eta e^{2i\delta} - 1)/2i$, we have

$$\delta \doteq \frac{1}{2}\tan^{-1}\frac{\eta_0 \sin 2\delta_0 + \eta_1 \sin 2\delta_1}{\eta_0 \cos 2\delta_0 + \eta_1 \cos 2\delta_1} \tag{12}$$

and

$$\eta = \frac{1}{2}\left[\eta_0^2 + \eta_1^2 + 2\eta_0\eta_1 \cos 2(\delta_0 - \delta_1)\right]^{1/2}, \tag{13}$$

which are respectively the lumped phase shift and absorption parameters. No effort was made to modify KAPANAL to take the different I-spin states of the K^--p system into account, because firstly it doubles the fitting parameters (which then surpass the number of experimental points, leaving no degree of freedom in data fitting), and secondly, without fitting charge-exchange angular distributions the two I-spin states cannot be distinguished. Therefore, rather than ambitiously aiming at a unique set of unambiguous phase-shift solutions, KAPANAL was used to find out what partial waves are needed to fit the differential cross section and polarization, and what particular behavior the lumped phase shift may display as a function of energy. The data of differential cross sections are taken from Bastien and Berge[5] (at 620, 760, and 850 MeV), Sodickson et al.[3] (at 1150 and 1260 MeV), and Holley[4] (the remaining 16 momenta in Table III).

The best χ^2 obtained at each momentum as a function of the numbers of partial waves used to fit the data are given in Table III (S_1 stands for $S_{1/2}$, P_1 stands for $P_{1/2}$, etc.). The numbers in parentheses are the expected χ^2's. The corresponding confidence levels and F-test results are given in Table IV. Several solutions with relatively smooth energy dependence were obtained. However, no especially notable behavior in phase shifts could be observed. It is possible that any significant structure in the phase shift of resonating single I-spin state (such as passing 90 deg at resonance) could be completely wiped out in the lumped phase shift because of the presence of the absorption parameter and the phase shift of the nonresonating I-spin state (Eq. 12).

B. Energy-Dependent Phase-Shift Analysis

A promising approach to the unique set of phase-shift solutions is by parameterizing the phase shifts, absorption parameters, and resonance parameters as functions of energy, rather than doing a single-energy phase-shift analysis and then trying to connect the single-energy phases together continuously as functions of energy. Such a scheme has achieved considerable success in p-p[26] and π-N scatterings,[27] and therefore suggests an enlightening application to K-N systems.

The 7094 program PIP, developed by Roper and Wright in their energy-dependent π-N phase-shift analysis,[27] has been recently modified for the K-N system by Bailey,[28] and was employed in this analysis. It is basically a grid search program which adjusts the variable parameters of relevant theoretical expressions to find the best fit to experimental data, or minimizes the χ^2 defined by

$$\chi^2 = \sum_i \left| \frac{0_i^c - 0_i^e}{\Delta\, 0_i^e} \right|^2 , \qquad (13)$$

Table III. χ^2 vs partial waves.

MeV/c	S_1	S_1P_1	$S_1P_1P_3$	$S_1P_1P_3D_3$	$S_1P_1P_3D_3D_5$	$S_1P_1P_3D_3D_5F_5$	$S_1P_1P_3D_3D_5F_5F_7$
620	35.0 (8)	3.0 (6)	3.0 (4)	1.0 (2)	2.4 (0)	1.5	1.1
700		71.0 (15)	15.0 (13)	12.5 (11)	10.8 (9)		
745		87.7 (17)	19.5 (15)	14.3 (13)	14.0 (11)		
760		35.0 (8)	2.0 (6)	1.8 (4)	1.4 (2)	1.5 (0)	1.2
775		104.2 (17)	16.6 (15)	16.4 (13)	15.3 (11)		
810		134.1 (16)	12.6 (14)	11.3 (12)	10.6 (10)	8.8 (8)	
835		153.2 (16)	23.7 (14)	21.1 (12)	18.6 (10)		
850			30.0 (10)	10.0 (8)	7.0 (6)	6.0 (4)	6.0 (2)
870		154.4 (16)	31.7 (14)	21.5 (12)	19.1 (10)	18.5 (8)	
905			53.9 (15)	30.8 (13)	25.0 (11)	19.3 (9)	13.9 (7)
940				38.9 (13)	24.6 (11)	14.1 (9)	11.5 (7)
985				98.8 (12)	53.1 (10)	17.5 (8)	16.1 (6)
1035					39.1 (11)	21.4 (9)	17.8 (7)
1085					31.4 (11)	19.5 (9)	17.5 (7)
1125				77.3 (12)	52.7 (10)	25.2 (8)	20.7 (6)
1150				25.0 (11)	17.0 (9)	17.0 (7)	16.4 (5)
1175				60.8 (13)	47.3 (11)	34.3 (9)	31.7 (7)
1225				49.6 (13)	18.5 (11)	18.1 (9)	20.7 (7)
1260				38.0 (11)	17.0 (9)	16.6 (7)	15.8 (5)
1290			164.4 (16)	79.9 (14)	54.2 (12)	49.2 (10)	48.3 (8)
1350			57.8 (17)	14.3 (15)	9.5 (13)	8.4 (11)	

The numbers in parenthesis are the expected χ^2s.

Table IV. Confidence levels for χ^2 and F test.

MeV/c	S_1	S_1P_1	$S_1P_1P_3$	$S_1P_1P_3D_3$	$S_1P_1P_3D_3D_5$	$S_1P_1P_3D_3D_5F_5$	$S_1P_1P_3D_3D_5F_5F_7$
620	0	88.5 (0)	70.0 (93)	80.0 (24)	12.5		
700		0	38.0 (4)	41.0 (15)	37.5 (18)		
745		0	25.0 (0)	43.0 (4)	30.0 (70)		
760		0	96.0 (0)	88.0 (51)	73.5 (42)	22.0	
775		0	41.5 (0)	29.0 (69)	22.5 (38)		
810		0	63.0 (0)	57.5 (24)	47.5 (43)	45.0 (22)	
835		0	7.0 (0)	7.0 (19)	7.0 (21)		
850			0	65.0 (2)	43.0 (13)	31.0 (41)	11.0 (100)
870		0	1.0 (0)	9.0 (3)	6.0 (26)	3.0 (60)	
905			0	2.0 (0)	4.0 (12)	3.5 (7)	8.5 (12)
940				0	1.0 (5)	16.5 (2)	17.5 (22)
985				0	0	4.0 (0)	2.5 (47)
1035					0	2.0 (2)	2.0 (24)
1085					0	3.5 (4)	2.5 (38)
1125				0	0	.25 (1)	.5 (25)
1150				1.5	7.5 (5)	3.0 (100)	1.0 (20)
1175				0	0 (9)	0 (8)	0 (34)
1225				0	10.0 (0)	5.5 (64)	.5 (100)
1260				0	7.5 (0)	3.5 (67)	1.5 (57)
1290			0	0 (0)	0 (4)	0 (32)	0 (69)
1350			0	57.5	80.0 (0)	75.0 (2)	0 (24)

The numbers in the parenthesis are the F-test confidence levels, namely the probabilities (%) of being correct in terminating at the lower fit.

where 0_i^e is the experimental measurement, 0_i^c is the value of the observable as calculated from the set of parameters in question, and $\Delta 0_i^e$ is the standard deviation pertaining to the experimental measurement. The index i is to be carried over all the pieces of data included in the analysis. In our case, the observables employed were total cross sections, differential cross sections, charge-exchange differential cross sections, and polarization angular distributions, for the K^--p system and K^--n total cross sections . The momentum of the incident K^- meson ranged from 110 to 1400 MeV/c. The list of references of all data used is given in Appendix C.

An outline of the parameterization of the scheme is the following. (For a full description and discussion of this scheme the reader is referred to reference 27.)

To account for the resonance behavior that might exist in some of the partial waves, the scattering amplitude was approximated by the sum of a resonant part and a nonresonant part,

$$A_{\ell\pm}^{(T)} = \epsilon\, A_{\ell\pm}^{(T)}\,(\mathrm{res}) + A_{\ell\pm}^{(T)}\,(\mathrm{nonres}), \qquad (14)$$

where T is the isotopic spin index, $\ell\pm$ stands for $\ell \pm 1/2$, and

$$\epsilon = \begin{cases} 1 \text{ for states in which we chose to put a resonance,} \\ 0 \text{ for states in which we do not put a resonance.} \end{cases}$$

(Henceforth, the isotopic spin superscript will be dropped for the sake of simplicity. Each quantity with subscript $\ell\pm$ is understood to also have a superscript T.)

For the resonant amplitude, Layson's relativistic Breit-Wigner form was employed:[29]

$$A_{\ell\pm}\,(\mathrm{res}) = \frac{-\,(1/2)\,\Gamma_{\mathrm{el}_{\ell\pm}}}{(q_0 - q_{0_{\ell\pm}}) + i\,(1/2)\,\Gamma_{t_{\ell\pm}}}\,; \qquad (15)$$

where q_0 is the total kaon c.m. energy, $q_{0_{\ell\pm}}$ is the resonance position, and

$$\Gamma_{t_{\ell\pm}} = \Gamma_{el_{\ell\pm}} + \Gamma_{in_{\ell\pm}} \tag{16}$$

is the total resonance width. The inelastic width is approximated by

$$\Gamma_{in_{\ell\pm}} = \overline{\Gamma}_{in_{\ell\pm}} \, k^{2\ell+1}, \tag{17}$$

where $\overline{\Gamma}_{in_{\ell\pm}}$ is the inelastic width of the individual resonance and k is the kaon c. m. momentum. The elastic width is given by

$$\Gamma_{el_{\ell\pm}} = \frac{4M}{q_0 + q_{0_{\ell\pm}}} \, k \, r_{0_{\ell\pm}} \, \gamma^2_{\ell\pm} \, \nu_\ell \, (k \, r_{0_{\ell\pm}}), \tag{18}$$

where M is the proton mass, r_0 is the interaction radius, $\gamma_{\ell\pm}$ is the reduced elastic width, and ν_ℓ is the barrier penetration factor:

$$\nu_\ell \, (k \, r_{0_{\ell\pm}}) = \frac{1}{k^2 \, r^2_{0_{\ell\pm}} \, [J^2_\ell \, (k \, r_{0_{\ell\pm}}) + N^2_\ell \, (k \, r_{0_{\ell\pm}})]}. \tag{19}$$

Here J_ℓ and N_ℓ are ℓ-th order Bessel and Neumann functions respectively.

For the nonresonant amplitude we have

$$A_{\ell\pm} \, (\text{nonres}) = \frac{\overline{\eta}_{\ell\pm} \, e^{2 i \overline{\delta}_{\ell\pm}} - 1}{2 i}, \tag{20}$$

with series expansion in powers of k for the nonresonant phase shifts and the absorption parameters:

$$\tan \overline{\delta}_{\ell\pm} = k^{2\ell+1} \sum_{n=0}^{\ell_m - \ell} (a_{\ell\pm})_n \, k^n \tag{21}$$

and

$$\overline{\eta}_{\ell\pm} = e^{-2\gamma} \tag{22}$$

where $$\gamma = k^{2\ell+1} \sum_{n=0}^{\ell_m - \ell} (b_{\ell\pm})_n \, k^n ; \tag{23}$$

ℓ_m is the highest partial wave employed.

For the actual phase shifts and absorption parameters, we have

$$\delta_{\ell\pm} = \frac{1}{2}\tan^{-1}\frac{2\,\mathrm{Re}\,A_{\ell\pm}}{1-2\,\mathrm{Im}\,A_{\ell\pm}} \tag{24}$$

and

$$\eta_{\ell\pm} = 2\left[(\mathrm{Re}\,A_{\ell\pm})^2 + (1/2 - \mathrm{Im}\,A_{\ell\pm})^2\right]^{1/2}, \tag{25}$$

where

$$\begin{aligned} A_{\ell\pm} &= \epsilon\, A_{\ell\pm}\,(\mathrm{res}) + A_{\ell\pm}\,(\mathrm{nonres}) \\ &= \frac{\eta_{\ell\pm}\, e^{2i\delta_{\ell\pm}} - 1}{2i} \end{aligned} \tag{26}$$

In order that unitarity be preserved, the following restrictions were made:

$$-1/2 \leq \mathrm{Re}\,A_{\ell\pm} \leq 1/2,\quad 0 \leq \mathrm{Im}\,A_{\ell\pm} \leq 1,\ \text{and}\ 0 \leq \eta_{\ell\pm} \leq 1.$$

With the above parameterization, we are ready to relate the partial-wave amplitude $A_{\ell\pm}$ to the experimental observables through the equations of scatterings, Eqs. (4) through (8) (Section IV. A). These equations hold for the charge-exchange scattering ($K^- + p \rightarrow \overline{K}^0 + n$) as well as for the elastic scattering. It has to be noted, however, that the elastic and charge-exchange scattering amplitudes have different isotopic spin decomposition, namely

$$A_{{el}_{\ell\pm}}{}^{(T)} = \frac{1}{2}\left(A_{\ell\pm}{}^{(1)} + A_{\ell\pm}{}^{(0)}\right) \tag{27}$$

and

$$A_{{cx}_{\ell\pm}}{}^{(T)} = \frac{1}{2}\left(A_{\ell\pm}{}^{(1)} - A_{\ell\pm}{}^{(0)}\right), \tag{28}$$

because the $\overline{K}^0$-n system decomposes into different $|T, T_3\rangle$ states by

$$|\overline{K}^0\, n\rangle = \frac{1}{\sqrt{2}}\left\{|1, 0\rangle - |0, 0\rangle\right\}.$$

One of the arguments for doing an energy-dependent phase-shift analysis is that fewer parameters are required than for single-energy phase-shift analysis. In the existing program, the parameters varied are the coefficients $(a_{\ell\pm})_n$, $(b_{\ell\pm})_n$ of Eqs. (21) and (23) respectively, the resonance position q_0 of Eq. (15), and the inelastic width $\overline{\Gamma}_{in_{\ell\pm}}$ of Eq. (17).

V. RESULTS AND DISCUSSION

The polarization of the recoil protons from K^--p elastic scattering was obtained at five incident kaon momenta (Figs. 13-B through 17-B). It appears that the polarization has generally similar angular dependence in the momentum region from 800 to 1050 MeV/c, positively polarized for protons recoiled forward in the laboratory system, and negatively polarized at 90 deg c.m. scattering angle. However, at 1159 MeV/c, just above the 1815-MeV resonance, the polarization has a drastic change in the angular dependence. There is also a remarkable change of polarization at 1266 MeV/c.

The result of the single-energy phase-shift analysis is summarized in Tables III and IV. As was mentioned in Section IV. A, the main purpose of this analysis is to explore what partial waves are sufficient to fit the differential cross sections and the polarizations. It is interesting to observe that there are abrupt decreases in χ^2 when certain partial waves are included. Incorporating the confidence levels and the F-test results in Table IV, one is inclined to conclude that those with underlined confidence levels are the best fits. Thus, at 620 MeV/c, S_1 and P_1 waves are sufficient to fit the data (here and henceforth S_1 stands for $S_{1/2}$, P_1 stands for $P_{1/2}$, etc.); at 700 MeV/c, the P_3 or possibly the D_3 wave is turned on; at 745 MeV/c, the D_3 wave is required; whereas from 760 to 835 MeV/c, the D_3 wave is no longer important. This probably reflects the presence of the D_{13} resonance at 715 MeV/c (here and henceforth the first subscript refers to the isotopic spin). From 850 to 905 MeV/c, the D_3 wave reappears. It is of special interest to observe that the F_5 wave is finite at momenta from 940 to 1125 MeV/c, while at higher momenta it is no longer required. This indicates the importance of the F_5 wave throughout the region of the 1815-MeV resonance, and is consistent with the F_5 assignment to this resonance. Apparently the D_5 wave does not play an important role at 940 MeV/c, where the 1765-MeV D_{15} resonance was suggested.[11] This fact implies the possibility of unimportance of the D_{15} resonance, if there is any, in the elastic channel. This agrees with the result of energy-dependent phase-shift analysis to be discussed below.

The above argument is, of course, only qualitative, and it cannot be used to rule out the possibility of interference between big D_{03} and small F_{07} background, for the data can also be fitted well with partial waves up to F_7.

The results of energy-dependent phase-shift analysis are summarized in Table V. In fitting the data in the momentum region from 110 to 1370 MeV/c, seven hypotheses were made. It is known that there are two resonances at 395 and 715 MeV/c. The resonating states are D_{03} and D_{13}, the masses are 1520 and 1660 MeV, and the full widths are 16 and 40 MeV, respectively. For the bump in the K^--p total cross section at 1050 MeV/c, we made two assumptions. Firstly, we assumed the bump to consist of a $T = 1$ resonance at 940 MeV/c (mass = 1765 MeV) and a $T = 0$ resonance at 1050 MeV/c (mass = 1815 MeV). Various spin and parity assignments were made to each resonance (Hypotheses 1 through 4). Secondly, we assumed the bump to be a single-state resonance, either F_{05}, D_{05}, or D_{03} (Hypotheses 5, 6, and 7). In fitting the data in the momentum region from 700 to 1370 MeV/c (concentrating in the 1050-MeV/c bump), four hypotheses were made (Hypotheses a, b, c, and d).

It is not very surprising to find a big χ^2 per degree of freedom, if one is familiar with the similar situation encountered in the energy-dependent phase-shift analysis of the π-p system.[27] As far as χ^2 is concerned, Hypotheses 1 and 2 seem to fit the existing data better than Hypotheses 3 and 4, Hypotheses 5 and 6 are better than Hypothesis 7, and Hypotheses a, b, and c are better than Hypothesis d. However, in view of the size of the χ^2, how strongly one can rule out D_{03} as a possible resonating state for the 1815-MeV bump could only be left open for individual judgment. It has to be pointed out that some solutions are not necessarily the best solutions obtainable for given sets of

Table V. Summary of results of energy-dependent phase-shift analysis.

Hypothesis	Resonating state	Mass (MeV)	Γ_{in} (MeV)	Γ_{el} (MeV)	Full width (MeV)	Number of data used	Number of fitted parameters	Expected χ^2	χ^2 Obtained	χ^2 per degree of freedom
1	D_{03}	1520	8.0	2.7	10.7	715	102	612	1355	2.21
	D_{13}	1660	31.2	6.1	37.3					
	D_{15}	1765	27.8	6.8	34.6					
	F_{05}	1820	21.6	48.3	69.9					
2	D_{03}	1522	7.0	2.9	9.9	715	102	612	1340	2.19
	D_{13}	1660	21.6	6.1	27.7					
	F_{15}	1765	106.0	9.8	115.8					
	D_{05}	1808	23.8	78.1	101.9					
3	D_{03}	1518	4.6	2.6	7.2	715	102	612	1809	2.95
	D_{13}	1660	625.3	6.1	631.4					
	D_{15}	1765	33.4	6.8	40.2					
	D_{03}	1815	10.3	81.2	91.5					
4	D_{03}	1518	4.6	2.6	7.2	715	102	612	1942	3.17
	D_{13}	1660	97.4	6.1	103.5					
	F_{15}	1765	94.6	9.8	104.4					
	D_{03}	1815	10.3	81.2	91.5					
5	D_{03}	1520	9.2	3.0	12.2	715	98	616	1357	2.20
	D_{13}	1708	59.2	17.6	76.8					
	F_{05}	1820	30.1	65.4	95.5					
6	D_{03}	1521	8.3	3.1	11.4	715	98	616	1342	2.18
	D_{13}	1679	50.6	13.3	63.9					
	D_{05}	1816	25.4	81.7	107.1					
7	D_{03}	1522	5.4	3.1	8.5	715	98	616	1704	2.76
	D_{13}	1752	138.1	25.0	163.1					
	D_{03}	1821	10.7	84.3	95.1					
a	D_{15}	1741	33.8	5.8	39.6	545	84	460	1173	2.54
	F_{05}	1811	22.1	44.3	66.4					
b	F_{05}	1807	31.1	58.3	89.4	545	82	462	1186	2.56
c	D_{05}	1807	19.6	77.3	96.9	545	82	462	1253	2.71
d	D_{03}	1815	10.3	81.2	91.5	545	82	462	1462	3.16

parameters. It is unfortunate that the existing data do not allow Hypothesis 1, 2, 5, and 6 to be differentiated from one another. Hypothesis 1, however, is in fair agreement with the suggested resonance parameters (except the 20% elasticity instead of suggested 60% elasticity[11] for the 1765-MeV resonance). The starting points for the varied parameters were so chosen that the correct behaviors of S-wave phase shifts were obtained at low energies where the S scattering lengths are known.[6] The final values of a and b coefficients for Hypothesis 1 are given in Tables VI and VII. The phase shifts and absorption parameters for different I-spin states as functions of K^- laboratory-system momentum are plotted in Figs. 18 through 21. It is interesting to note that the phase shifts of D_{03}, D_{13}, and D_{15} resonances pass through 0 deg, whereas that of the F_{05} resonance passes through 90 deg at the respective resonant energies. The former is the characteristic for resonances dominant in inelastic channels ($\Gamma_{in} > \Gamma_{el}$), while the latter is for the resonance dominant in the elastic channel. The S-wave phase shifts are in qualitative agreement with those obtained by Watson et al. at low energies.[6] It is of no special significance that the S_{01} phase shift stays at 90 deg above 400 MeV/c, because this partial wave becomes very strongly absorptive, as is shown in Fig. 20.

As is well known, there are two fundamental ambiguities (Minami and sign ambiguities) in the phase-shift solutions that satisfy the differential cross section.[23] This is because the differential cross section $\sigma(\theta)$ is invariant under the following transformations. For convenience, we can write symbolically,

$$M\sigma(\theta,\ \delta) = \sigma(\theta,\ \delta_M) = \sigma(\theta,\ \delta),$$

$$S\sigma(\theta,\ \delta) = \sigma(\theta,\ \delta_S) = \sigma(\theta,\ \delta),$$

where M and S are the Minami and sign operators which transform the parity ($\omega \rightarrow -\omega$) and the sign ($\delta \rightarrow -\delta$) of the real parts of the phase shifts, respectively, provided the substitution is carried out simultaneously for all isotopic spins and total angular momenta. In other

Table VI. Phase-shift coefficients.

$$\tan \bar{\delta}_{\ell\pm} = k^{2\ell + 1} \sum_{n=o}^{\ell_m-\ell} (a_{\ell\pm})_n k^n$$

Phase	a_1	a_2	a_3	a_4	a_5	a_6
S_{01}	+4.274973	-2.349084	-36.015902	+1.887917	+287.33020	+1238.540466
S_{11}	+1.017337	+1.466428	+0.021567	-0.501341	-0.555352	
P_{01}	-1.271372	+0.577978	+1.406650	+0.970320		
P_{11}	+0.455082	+0.191525	-0.404729	+0.377788		
P_{03}	+0.521368	-0.030083	-0.161380	-0.083437		
P_{13}	+0.310102	+0.003268	-0.092854	-0.073453		
D_{03}	-0.120573	-0.058661	+0.111007			
D_{13}	+0.042974	-0.041049	-0.046597			
D_{05}	+0.005731	+0.021226	+0.002469			
D_{15}	-0.141769	+0.034152	+0.040347			
F_{05}	-0.180522	+0.133445				
F_{15}	+0.074184	-0.042534				
F_{07}	-0.086134	+0.069106				
F_{17}	-0.101359	+0.076780				

Table VII. Absorption coefficients.

$$\bar{\eta}_{\ell\pm} = e^{-2\gamma}, \ \gamma = k^{2\ell + 1} \sum_{n=o}^{\ell_m - \ell} (b_{\ell\pm})_n \, k^n$$

Phase	b_1	b_2	b_3	b_4	b_5	b_6
S_{01}	+1.501728	-1.053370	-0.897859	+1.321766	+1.004362	-0.998192
S_{11}	+0.516296	+0.040689	-0.161517	-0.081827	-0.029369	
P_{01}	+0.625323	-0.170930	-0.152730	-0.206436		
P_{11}	+0.021264	-0.075478	-0.003986	+0.184072		
P_{03}	+0.319907	-0.101775	-0.066863	-0.026608		
P_{13}	+0.011992	+0.165694	-0.042220	-0.061528		
D_{03}	+0.	+0.	+0.			
D_{13}	+0.028827	-0.020843	+0.			
D_{05}	+0.019125	-0.012452	+0.			
D_{15}	+0.083964	+0.	-0.046018			
F_{05}	+0.000843	+0.				
F_{15}	+0.008842	+0.025400				
F_{07}	+0.					
F_{17}	+0.					

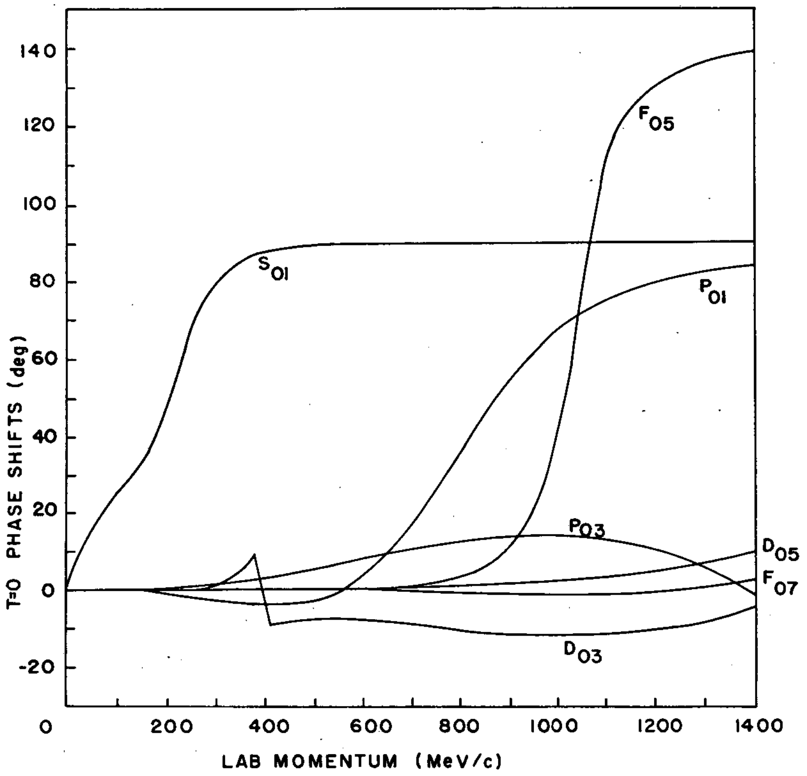

MU-35359

Fig. 18. Energy dependence of the T=0 phase shifts for Hypothesis 1.

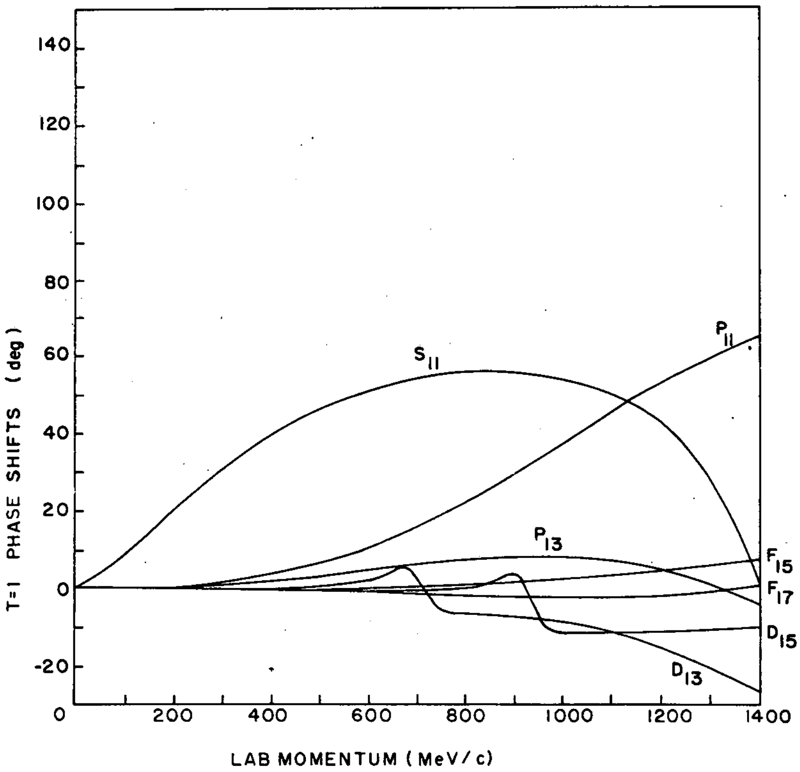

MU-35357

Fig. 19. Energy dependence of the T=1 phase shifts for Hypothesis 1.

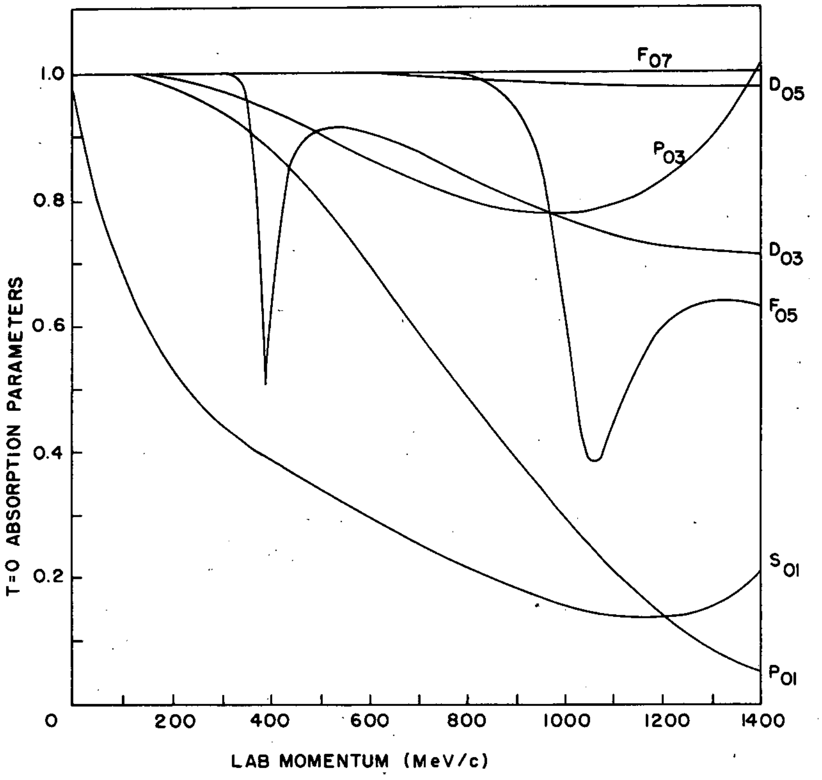

MU-35358

Fig. 20. Energy dependence of the T=0 absorption parameters for Hypothesis 1.

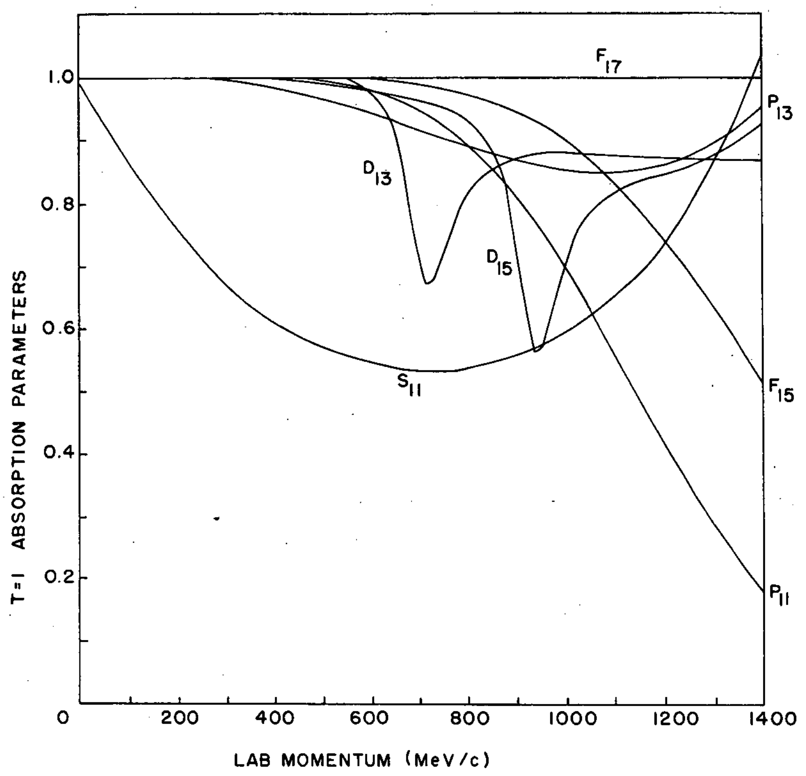

MU-35356

Fig. 21. Energy dependence of the T=1 absorption parameters for Hypothesis 1.

words, M and S transform δ into δ_M and δ_S (= $-\delta$), respectively, where all δ's are to be understood as standing for the complete set of phase-shift solutions. Nevertheless, the polarization $P(\theta)$ changes sign under these transformations,

$$MP(\theta, \delta) = P(\theta, \delta_M) = -P(\theta, \delta),$$

$$SP(\theta, \delta) = P(\theta, \delta_S) = -P(\theta, \delta).$$

This property essentially constitutes one of the principal attractions in carrying out a polarization experiment. Polarization alone, however, does not suffice to exclude all ambiguities, since successive Minami and sign transformations leave polarization invariant:

$$MSP(\theta, \delta) = SMP(\theta, \delta) = -SP(\theta, \delta_M) = P(\theta, -\delta_M) = P(\theta, \delta).$$

Fortunately, this ambiguity can further be eliminated by checking the sign of the real part of the forward scattering amplitude $D(0)$.[30] From Eq. (4), $D(0)$ can be written as

$$D(0) = \frac{\lambda}{2k} \sum [(\ell + 1)\eta_{\ell+} \sin 2\delta_{\ell+} + \ell\, \eta_{\ell-} \sin 2\delta_{\ell-}].$$

It is then easy to see that the following relations hold:

$$MD(0, \delta) = D(0, \delta_M) = D(0, \delta),$$

$$SD(0, \delta) = D(0, -\delta) = -D(0, \delta);$$

therefore

$$MSD(0, \delta) = D(0, -\delta_M) = -D(0, \delta_M).$$

In short, four sets of ambiguous solutions, δ, δ_M, δ_S, and $-\delta_M$, obtainable from fitting differential cross sections, can be reduced to two sets, δ and $-\delta_M$, by polarization measurement; furthermore, this ambiguity can be eliminated by comparing the sign of the real part of the forward scattering amplitude, calculated from the phase-shift solution and that obtained by use of forward dispersion relations.

The curves in Figs. 22 through 26 show the polarization calculated by the phase-shift solution of Hypothesis 1. The agreement with

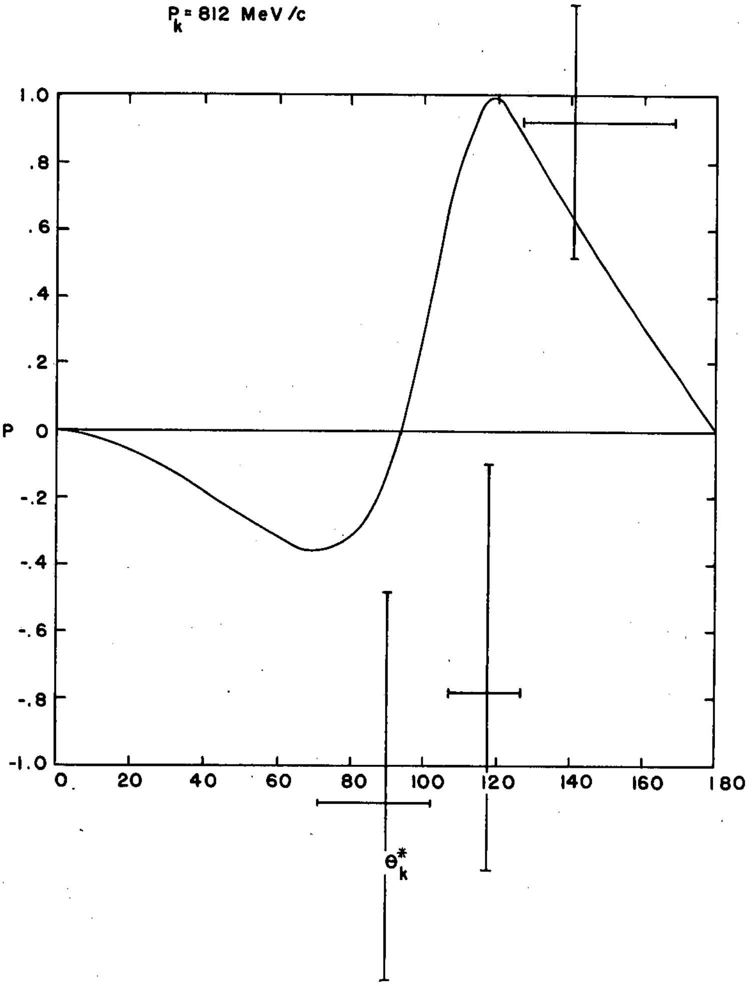

MU-35383

Fig. 22. The polarization calculated from the phase-shift solution of Hypothesis 1 versus data from this experiment.

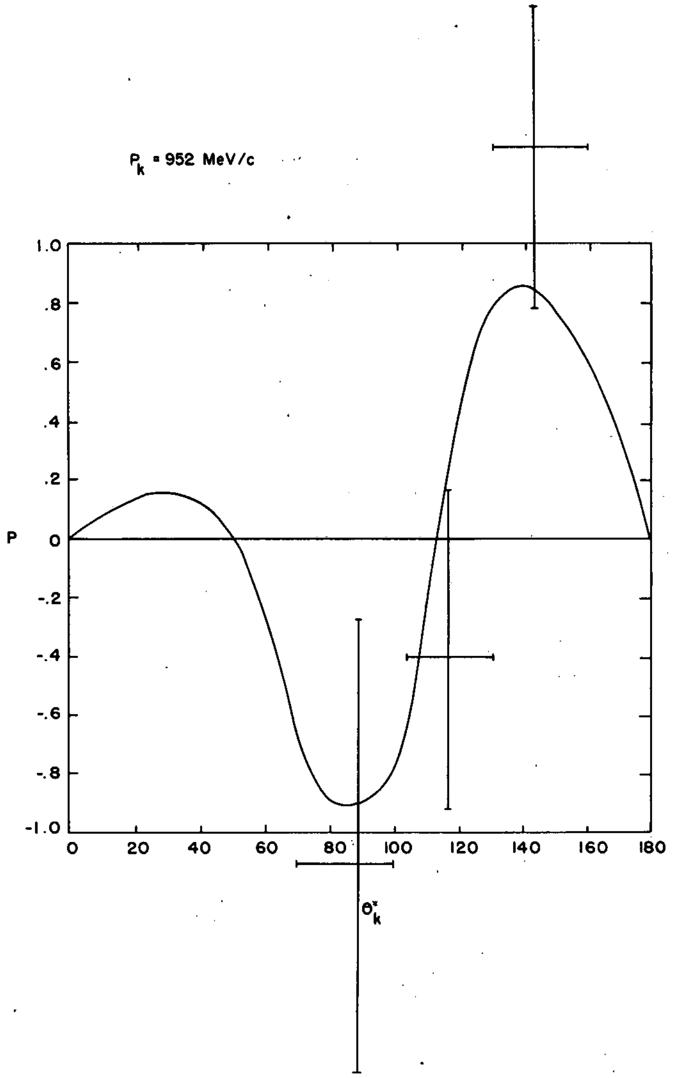

MU-35385

Fig. 23. The polarization calculated from the phase-shift solution of Hypothesis 1 versus data from this experiment.

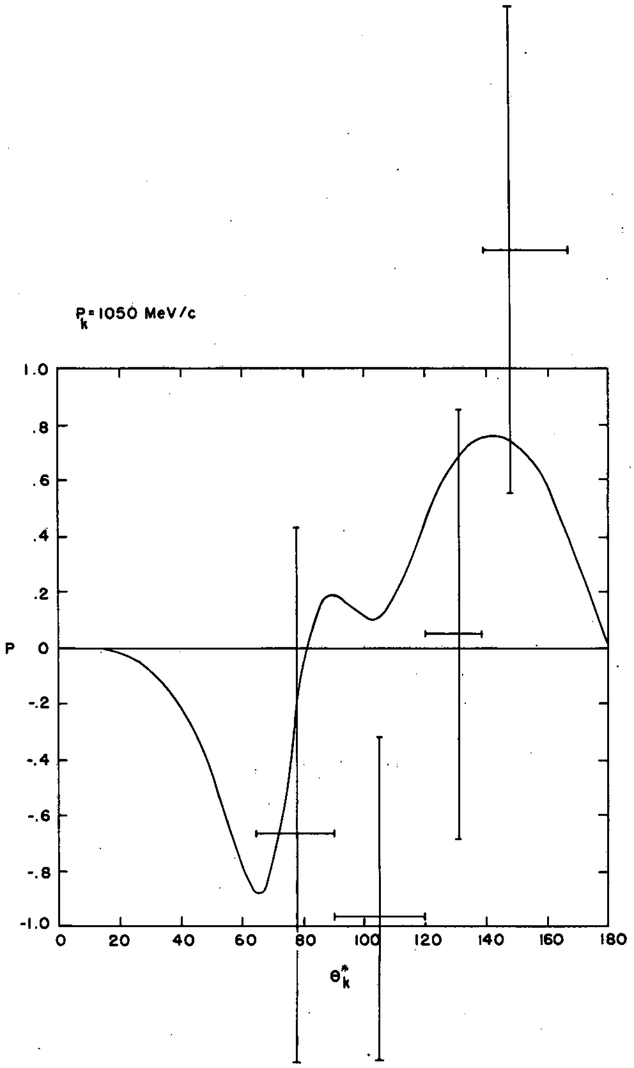

Fig. 24. The polarization calculated from the phase-shift solution of Hypothesis 1 versus data from this experiment.

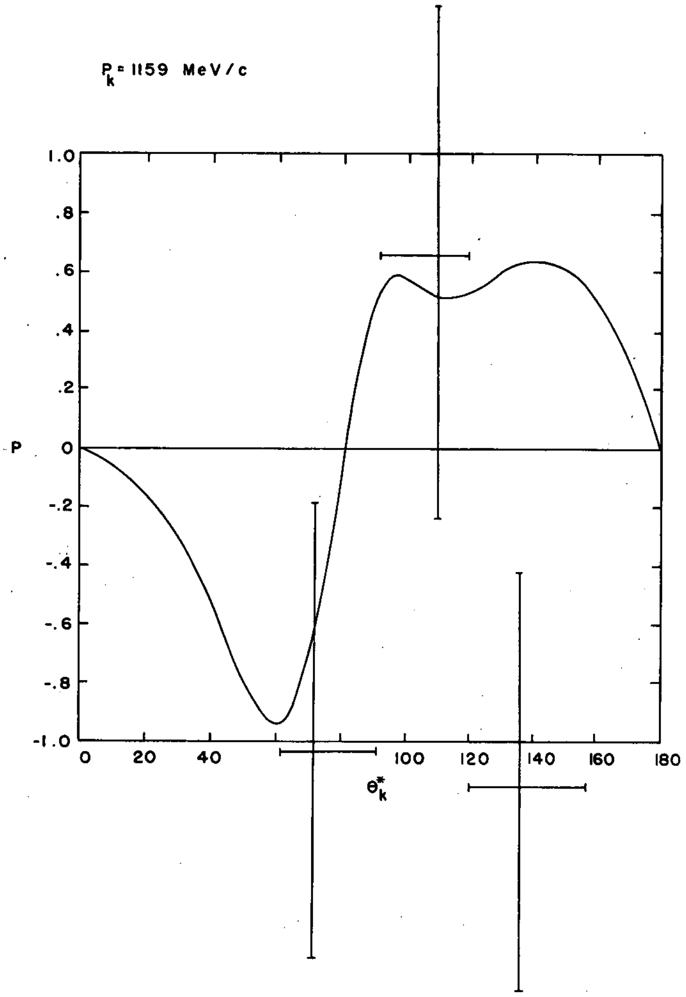

Fig. 25. The polarization calculated from the phase shift solution of Hypothesis 1 versus data from this experiment.

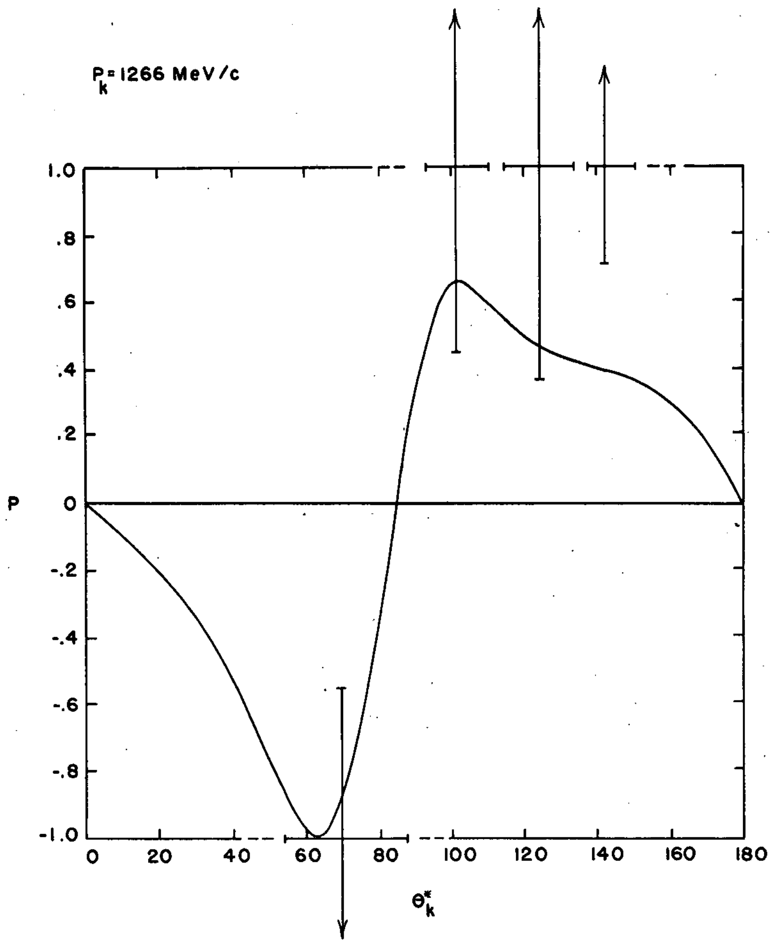

Fig. 26. The polarization calculated from the phase-shift solution of Hypothesis 1 versus data from this experiment.

the experimental points is reasonable if all fits are considered as a whole. Figure 27 shows the comparison between the two dispersion curves. Curve D_E is the real part of the forward scattering amplitude, calculated from the same solution, while curve D_C was replotted from the curves given by Cook et al.[31] using K-N forward dispersion relations. The agreement between the two curves is fair, except at low energies and at energies near 900 MeV. The reasonable fit of the phase-shift solution to both polarization and dispersion curves indicate that the solution has no Minami and sign ambiguities. This is because in the energy-dependent phase-shift analysis, the search program started from points where the behaviors of some phase shifts are known; besides, the spins and parities of some resonances are known. The curves in Fig. 1 are, from top to bottom, the K^--p, K^--n total cross sections and K^--p elastic cross sections respectively, as calculated from the solution of Hypothesis 1.

In conclusion, the results of both single-energy and energy-dependent phase-shift analyses are in favor of the F_{05} assignment to the 1815-MeV bump in the K^--p total cross section. This is in agreement with our previous preliminary investigation[16] (and later confirmed by Sodickson et al.[3]) of the elastic differential cross sections in terms of the cosine series expansion coefficients. This assignment would then agree with the predictions of the global symmetry model,[8] the Regge trajectory, and the SU_3 unitary symmetry scheme.[10] Though the result of the energy-dependent phase-shift analysis is in agreement with the conjecture of two resonances (D_{15} resonance at 1765 MeV and F_{05} resonance at 1815 MeV; Hypothesis 1), it is unfortunately impossible to exclude other possibilities (Hypotheses 2, 5, and 6). In this respect, and also for other reasons, the phase-shift solution obtained here is merely a possible solution and is by no means to be taken as a unique set. More data in K^--p charge exchange differential cross sections in the resonance region should be of great help in clarifying the situation, because the scattering amplitude in this channel is the

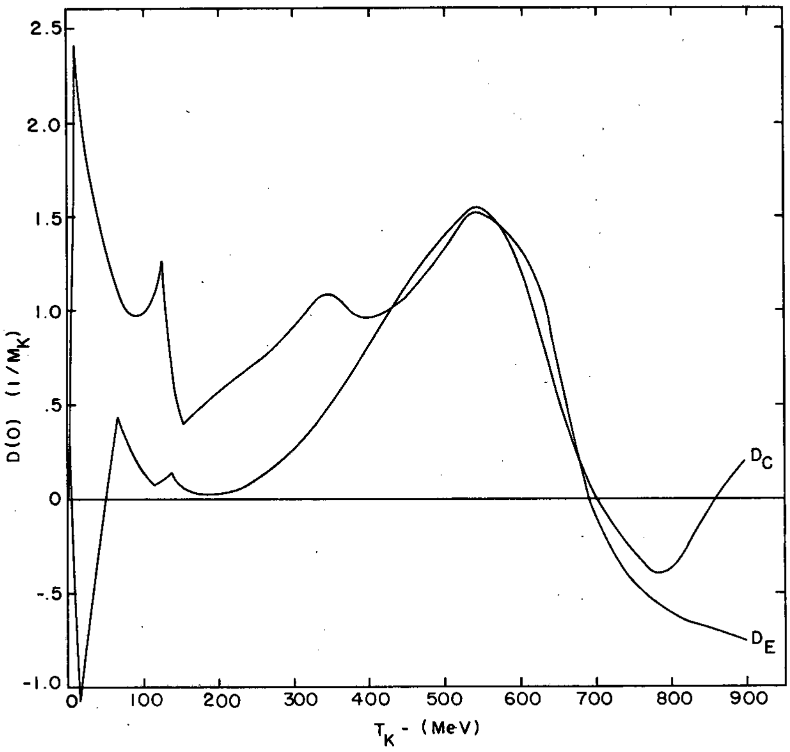

MU-35355

Fig. 27. Comparison of the real part of the forward scattering amplitude for K^--p scattering as calculated from the phase-shift solution of Hypothesis 1 (D_E) and as calculated by the forward dispersion relations (D_C, reference 30).

destructive superposition of the two different I-spin amplitudes, as compared with the constructive superposition in the case of elastic scattering (see Eqs. 27 and 28 of Section IV. B). More extensive study of the energy-dependent phase-shift analysis is being carried out by Bailey,[28] using the preliminary charge-exchange data from the Powell-Birge group of the Lawrence Radiation Laboratory. More polarization data with higher accuracy would always be useful in distinguishing different solutions. Detailed measurement of the K^--n total cross section (pure $I = 1$ state) in the resonance region, of course, yields the most clear-cut judgment regarding the existence of the 1765-MeV D_{15} resonance.

ACKNOWLEDGMENTS

It is with great pleasure that the author acknowledges the guidance and encouragement of Dr. Bruce Cork, Dr. Denis Keefe, Professor Leroy T. Kerth and Dr. William A. Wenzel during his graduate career. Many thanks are due to Dr. Edward J. Lofgren, Professor Robert L. Thornton, Dr. Donald Cooksey, and Professor A. C. Helmholz for their hospitality and advice.

The author is indebted to Mr. William R. Holley, Dr. Victor Cook, Dr. Edgar Beall, Dr. John Thresher, and Dr. William Layson for valuable discussions and suggestions during the analysis of the data. The assistance of Mr. Jack Camiel, Mr. Daniel R. George, and Mr. James E. Bourinskie in various phases of the data analysis is deeply appreciated. The author thanks Mr. Dave Baily for loan of his modified PIP program and for many discussions. Thanks are due to Dr. Richard D. Eandi for loan of his Polarization Program containing carbon analyzabilities, as well as for supplying analyzability data at higher energies before publication. The efforts of Mr. Carl Burton, Mr. Robert Duncan, Mr. William Hallum, Mr. D. Linn, and Mr. Gerald L. Schnurmacher for setting up and running the experiment; and of Mr. D. Barefoot, Mr. Wilson Blake, Mr. Ray Cunan, Mr. Frederick R. Goozen, Mr. Jerry Greenwood, Miss Fay Harrington, Mr. William H. Hetzel, Mr. W. Leak, Mr. Robert W. Miller, and Mrs. Barbara J. Quinn for scanning the film are greatly appreciated. For the rapid and careful typing of the preliminary manuscript, the author is grateful to Miss Anna Mae Naranjo.

The experiment would not have been possible without the generous contributions of time and effort by many groups of people. The spark chambers were constructed by the accelerator technicians, help in setting up the K^- beam was furnished by the Bevatron operation crew and staff, and efficient computer facilities were provided by the Math-Computing group. It has been a pleasure to work in the cooperative and pleasant atmosphere of the whole laboratory under the directorship of Professor Edward M. McMillan.

This work was done under the auspices of the U. S. Atomic Energy Commission.

APPENDICES

A. Analyzability of Carbon

The data on the analyzability of carbon used for the present data analysis comes from two sources.

For protons with energy below 325 MeV, the analyzability was taken from the graph furnished by Peterson.[20] It is reproduced in Fig. A-1. The variables $\theta^{*} = \theta\ (E/180\ \text{MeV})^{1/2}$ and $P^{*} = P/P_{max}$ were chosen in order to factor out the rapid variation of P with energy and angle; θ is the laboratory-system angle of p-C scattering for unpolarized incident protons, and P_{max} is the maximum polarization for each energy. When carbon is used as an analyzer P of course becomes the analyzability. This curve includes inelastic scatterings up to 50 MeV energy loss in p-C scatterings.

For protons whose incident energy is above 325 MeV, the analyzability of carbon was taken from the table furnished by Eandi.[21] It is reproduced in Table A-I. The analyzability includes all inelastic p-C scatterings.

B. Comparison of Likelihood Functions for Constant versus Linear Approximation in Polarization Estimation.

In estimating polarization P by the maximum-likelihood function

$$L\ (P) = \prod_i (1 + PA_i \cos \theta_i),$$

P is usually assumed to be constant within certain angular intervals of K^--p scattering. (A) and (C) of Fig. B-1 show the polarization and the maximum-likelihood function obtained in this way.

P is in fact better approximated by a linear function of the K^--p scattering angle. (D) of Fig. B-1 shows that the maximum-likelihood function obtained by this method is considerably higher than that obtained by the constant approximation (C). The solid line of (B) shows the linearly approximated polarization and the broken lines show the error limits at which the likelihood function decreases to $e^{-1/2}$ of its peak value.

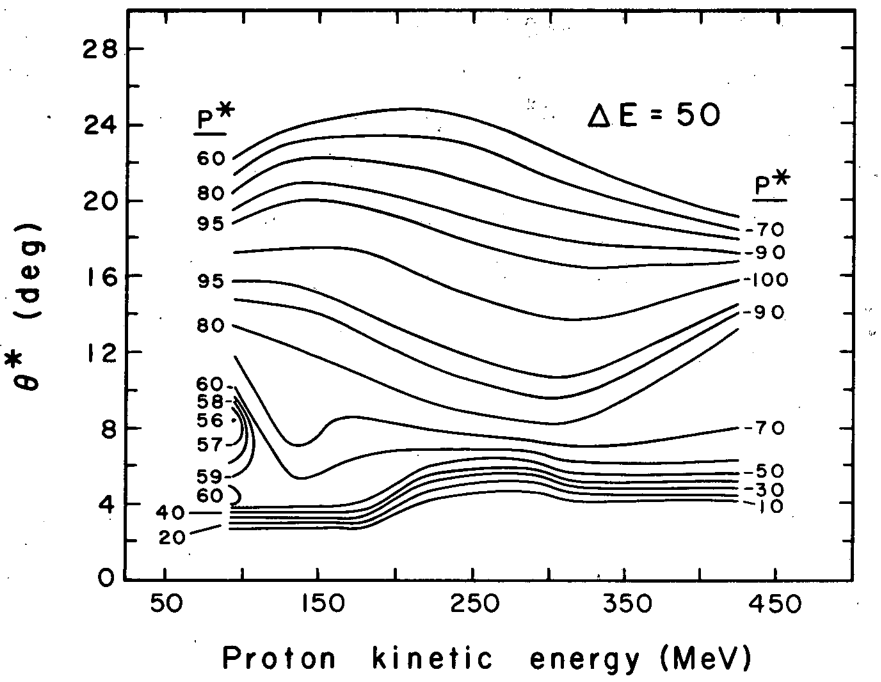

MU-29523

Fig. A-1. Normalized contour plot of analyzability of carbon (reference 20), if inelastic scatterings up to 50 MeV energy loss are included. The contours are lines of constant P* expressed in percent. (For definitions see text.)

Table A-I. p-C Analyzability (from reference 21)
(Including inelastic scatterings)

θ/T	440	460	480	500	520	540
5.0	0.15±.16	0.32±.14	0.24±.12	0.18±.10	0.25±.09	0.20±.08
6.0	0.22±.12	0.37±.10	0.33±.08	0.22±.08	0.26±.06	0.20±.08
7.5	0.36±.10	0.37±.09	0.42±.08	0.34±.07	0.26±.06	0.24±.06
9.0	0.37±.09	0.32±.09	0.36±.08	0.38±.08	0.25±.06	0.26±.06
10.5	0.27±.10	0.24±.09	0.31±.08	0.31±.07	0.23±.07	0.25±.06
12.0	0.31±.10	0.26±.09	0.27±.08	0.30±.08	0.28±.08	0.25±.07
13.5	0.34±.10	0.35±.10	0.34±.09	0.35±.09	0.35±.08	0.33±.07
15.0	0.39±.12	0.44±.10	0.35±.10	0.35±.09	0.35±.08	0.40±.07
16.5	0.39±.12	0.39±.10	0.23±.10	0.17±.10	0.23±.09	0.31±.08
18.0	0.20±.12	0.25±.12	0.26±.10	0.17±.10	0.17±.09	0.30±.09
21.0	0.24±.10	0.33±.11	0.36±.10	0.23±.10	0.27±.09	0.27±.09
24.0	-0.03±.10	-0.05±.12	0.22±.11	0.29±.10	0.20±.10	0.26±.09

θ/T	560	580	600	620	640
5.0	0.19±.08	0.19±.06	0.20±.06	0.30±.06	0.36±.07
6.0	0.18±.06	0.18±.06	0.25±.06	0.35±.05	0.42±.06
7.5	0.20±.06	0.20±.06	0.31±.05	0.40±.05	0.44±.05
9.0	0.26±.05	0.23±.06	0.32±.05	0.40±.05	0.46±.06
10.5	0.38±.06	0.26±.06	0.30±.05	0.35±.05	0.41±.06
12.0	0.21±.07	0.18±.06	0.26±.06	0.32±.06	0.38±.07
13.5	0.29±.07	0.22±.07	0.30±.06	0.38±.06	0.40±.07
15.5	0.30±.07	0.24±.07	0.27±.06	0.34±.06	0.35±.07
16.5	0.28±.07	0.24±.07	0.24±.06	0.30±.06	0.33±.07
18.0	0.20±.08	0.20±.07	0.20±.07	0.27±.06	0.36±.08
21.0	0.16±.08	0.12±.07	0.18±.07	0.33±.07	0.32±.09
24.0	0.12±.09	0.15±.08	0.26±.08	0.22±.08	0.33±.09

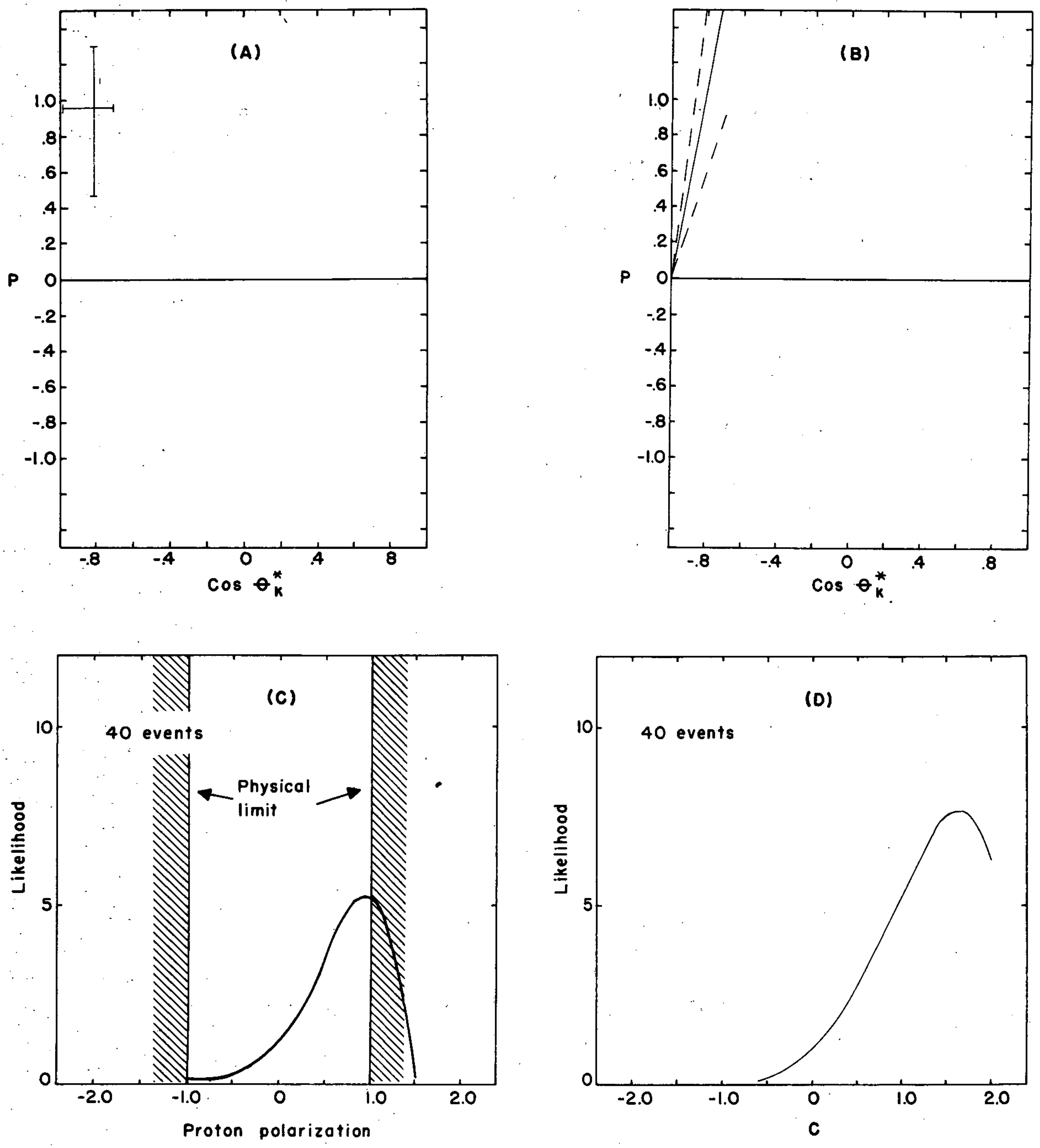

MUB-4974

Fig. B-1. Comparison of the constant versus the linear approximations in calculating the polarization. In A and C, polarization is assumed constant within an angular region. In B and D, the polarization is assumed to be a linear function of $\cos\theta_k{}^*$ within the same angular region as A and C.

C. References of Data Used in Energy-Dependent Phase-Shift Analysis

1. Bruce Cork, G. Lambertson, O. Piccioni, and W. Wenzel, Phys. Rev. 106, 167 (1957)
2. A. H. Rosenfeld, Bull. Am. Phys. Soc. 3, 363 (1958).
3. H. Burrowes, D. Caldwell, D. Frisch, D. Hill, D. Ritson, and R. Schulter, Phys. Rev. Letters 2, 117 (1959).
4. L. Alvarez, Report on Strange Particle Interactions, in Proceedings of the Ninth International Conference on High Energy Physics, Kiev, 1959.
5. S. C. Freden, F. Gilbert, and R. White, Phys. Rev. Letters 4, 265 (1960).
6. P. Bastien, O. Dahl, D. Miller, J. Murray, F. Solmitz, and R. Tripp, Bull. Am. Phys. Soc. 5, 509 (1960).
7. G. von Dardel, D. Frisch, R. Mermod, R. Millburn, P. Piroué, M. Vivargent, G. Weber, and K. Winter, in Proceedings of the 1960 Annual International Conference on High Energy Physics, Rochester.
8. H. Going, Nuovo Cimento 16, 848 (1960).
9. V. Cook, B. Cork, T. Hoang, D. Keefe, L. Kerth, W. Wenzel, and T. Zipf, Phys. Rev. 123, 320 (1961).
10. S. Goldhaber, G. Goldhaber, W. Powell, and R. Silberberg, Phys. Rev. 121, 1525 (1961).
11. Ronald R. Ross, Elastic and Charge-Exchange Scattering of K^- Mesons in Hydrogen (Ph. D. Thesis), UCRL-9749, June 1961.
12. O. Chamberlain, K. Crowe, D. Keefe, L. Kerth, A. Lemonick, T. Maung, and T. Zipf, Phys. Rev. 125, 1696 (1962).
13. W. Baker, R. Cool, E. Jenkins, T. Kycia, R. Phillips, and A. Read, Phys. Rev. 129, 2285 (1963).
14. M. Watson, M. Ferro-Luzzi, and R. Tripp, Phys. Rev. 131, 2248 (1963).
15. Pierre L. Bastien, K^--Proton Interactions Near 760 MeV/c (Ph. D. Thesis), UCRL-10779, Feb. 1963.

16. L. Sodickson, I. Mannelli, D. Frisch, and M. Wahlig, Phys. Rev. 133-B, 757 (1964).
17. C. Wohl, Alvarez Group Physics Notes, 517, Lawrence Radiation Laboratory (unpublished).
18. W. Graziano and S. G. Wojcicki, Phys. Rev. 128, 1868 (1962).
19. William Holley, K^--Proton Elastic Scattering in the Momentum Range 700 to 1400 MeV/c (Ph.D. Thesis), in preparation.

REFERENCES

1. V. Cook, Bruce Cork, T. F. Hoang, D. Keefe, L. T. Kerth, W. A. Wenzel, and T. F. Zipf, Phys. Rev. 123, 320 (1961).
2. O. Chamberlain, K. M. Crowe, D. Keefe, L. T. Kerth, A. Lemonick, Tin Maung, and T. F. Zipf, Phys. Rev. 125, 1696 (1962).
3. L. Sodickson, I. Mannelli, D. Frisch, and M. Wahlig, Phys. Rev. 133, B757 (1964).
4. William Holley, K^--Proton Elastic Scattering in the Momentum Range 700 to 1400 MeV/c (Ph. D. Thesis), in preparation.
5. P. L. Bastien and J. P. Berge, Phys. Rev. Letters 10, 188 (1963).
6. Mason B. Watson, Massimiliano Ferro-Luzzi, and Robert D. Tripp, Phys. Rev. 131, 2248 (1963).
7. R. H. Dalitz, Three Lectures on Elementary Particles Resonances (Brookhaven National Laboratory, Upton, N. Y., 1961) p. 32.
8. Leroy T. Kerth and Abraham Pais, On the Gentle Art of Hunting Bumps in the Pion-Hyperon System, UCRL-9706, May 1961 (unpublished).
9. J. S. Ball and W. R. Frazer, Phys. Rev. Letters 7, 204 (1961); William R. Frazer and Archibald W. Hendry, Phys. Rev. 134, B1307 (1964).
10. Sheldon L. Glashow and Arthur Rosenfeld, Phys. Rev. Letters 10, 192 (1963).
11. A. Barbaro-Galtieri, A. Hussain, and R. D. Tripp, Phys. Letters 6, 296 (1963).
12. W. S. C. Williams, An Introduction to Elementary Particles (Academic Press, Inc., New York, 1961), Chap. VIII.
13. H. Cramer, Mathematical Methods of Statistics (Princeton University Press, Princeton, New Jersey, 1958), p. 498.

14. Bruce Cork, Denis Keefe, and William A. Wenzel, A Coincidence-Anticoincidence Gas Cerenkov Counter, in Proceedings of an International Conference on Instrumentation for High-Energy Physics (Interscience Publishers, New York 1960), p. 84.

15. E. F. Beall, W. Holley, D. Keefe, L. T. Kerth, J. J. Thresher, C. L. Wang, and W. A. Wenzel, Nucl. Instr. Methods 20, 205 (1963).

16. E. F. Beall, W. Holley, D. Keefe, L. T. Kerth, J. J. Thresher, C. L. Wang and W. A. Wenzel, in Proceedings of the International Conference on High-Energy Nuclear Physics, Geneva, 1962 (CERN Scientific Information Service, Geneva, Switzerland, 1962), p. 368.

17. J. C. Hodges, D. Keefe, L. T. Kerth, J. J. Thresher, and W. A. Wenzel, Digitized Measuring Projector for the Analysis of Spark-Chamber Photographs, UCRL-10251, May 1962 (unpublished).

18. John H. Atkinson, Jr., and Beverly Hill Willis, High Energy Particle Data. II, UCRL-2426 (rev.), 1956 (unpublished).

19. Robert W. Birge and William B. Fowler, Phys. Rev. Letters 5, 254 (1960).

20. Vincent Z. Peterson, Analyzing Power of Carbon for High-Energy Polarized Protons, UCRL-10622, Sept. 1963 (unpublished).

21. Richard D. Eandi (Lawrence Radiation Laboratory), private communication.

22. J. M. Dickson, B. Rose, and D. C. Salter, Proc. Phys. Soc. (London) A, 58, 361 (1955); J. J. Thresher, private communication.

23. Hans A. Bethe and Frederic deHoffmann, Mesons and Fields, II (Row, Peterson and Co., Evanston, Illinois, 1956), p. 63.

24. J. H. Foote, Scattering of Positive Pions on Protons at 310 MeV: Recoil Nuclear Polarization and Phase Shift Analysis (Ph. D. Thesis), UCRL-9191, Sept. 1960 (unpublished).

25. Victor Cook, K^+-Nucleon Interactions in the Momentum Range of 800 to 2900 MeV/c (Ph. D. Thesis), UCRL-10130, March 1962 (unpublished).

26. M. H. MacGregor, M. J. Moravcsik, and H. P. Stapp, Ann. Rev. Nucl. Sci. 10, 291 (1960).

27. L. David Roper and Robert M. Wright, UCRL-7846, 1964 (unpublished); L. David Roper, Pion-Nucleon Phase Shift Analysis From 0 to 1.5 BeV (Ph. D. Thesis), Massachusetts Institute of Technology, 1963 (unpublished).

28. Dave Bailey (Lawrence Radiation Laboratory), private communication.

29. B. T. Feld and W. M. Layson, in Proceedings of the International Conference on High-Energy Nuclear Physics, Geneva, 1962 (CERN Scientific Information Service, Geneva, Switzerland, 1962), p. 147; W. M. Layson, Nuovo Cimento 27, 724 (1963).

30. H. L. Anderson, W. C. Davidon, and U. E. Kruse, Phys. Rev. 100, 339 (1955).

31. V. Cook, D. Keefe, L. T. Kerth, P. G. Murphy, W. A. Wenzel, and T. F. Zipf, Phys. Rev. 129, 2743 (1963).